Interstellar Hydrides

Maryvonne Gerin,[1,2] David A. Neufeld,[3,4] and Javier R. Goicoechea[5]

[1]LERMA, Observatoire de Paris, PSL Research University, CNRS, UMR8112, Paris F-75014, France; email: maryvonne.gerin@ens.fr

[2]Sorbonne Universités, UPMC Paris 06, UMR8112, LERMA, Paris F-75005, France

[3]Department of Physics and Astronomy, Johns Hopkins University, Baltimore, Maryland 21218; email: neufeld@jhu.edu

[4]Astronomy Department, University of Maryland, College Park, Maryland 20742

[5]ICMM, Consejo Superior de Investigaciones Cientificas, E-28049 Madrid, Spain; email: jr.goicoechea@icmm.csic.es

Annu. Rev. Astron. Astrophys. 2016. 54:181–225

First published online as a Review in Advance on July 22, 2016

The *Annual Review of Astronomy and Astrophysics* is online at astro.annualreviews.org

This article's doi: 10.1146/annurev-astro-081915-023409

Keywords

interstellar medium, interstellar molecules, molecular ions, astrochemistry, molecular spectroscopy

Abstract

Interstellar hydrides—that is, molecules containing a single heavy element atom with one or more hydrogen atoms—were among the first molecules detected outside the solar system. They lie at the root of interstellar chemistry, being among the first species to form in initially atomic gas, along with molecular hydrogen and its associated ions. Because the chemical pathways leading to the formation of interstellar hydrides are relatively simple, the analysis of the observed abundances is relatively straightforward and provides key information about the environments where hydrides are found. Recent years have seen rapid progress in our understanding of interstellar hydrides, thanks largely to FIR and submillimeter observations performed with the *Herschel Space Observatory*. In this review, we discuss observations of interstellar hydrides, along with the advanced modeling approaches that have been used to interpret them and the unique information that has thereby been obtained.

Contents

1. INTRODUCTION

1.1. Historical Perspective

ISM: interstellar medium

Although dust and gas clouds were suspected to exist early in the twentieth century, the survival of molecules in the harsh interstellar medium (ISM) was more controversial (e.g., Eddington 1926). Together with CN, the hydrides CH and CH^+ were the first gas-phase molecules detected in the 1930s and 1940s (e.g., Swings & Rosenfeld 1937, Douglas & Herzberg 1941). The improved spectral resolution of visible light spectrometers allowed the detection of very narrow absorption

lines in the spectra obtained toward nearby and bright stars. Their associated wavelengths were well known to molecular spectroscopists and the small line widths suggested low gas temperatures, much lower than those of the stellar atmospheres producing broad atomic features. Indeed, the observed narrow lines remained stationary in the spectra of spectroscopic binary stars whose photospheric lines showed periodic velocity shifts. Today such absorption lines are understood as being produced by diffuse interstellar clouds [with gas densities, defined as $n_H = n(H) + 2n(H_2)$, of less than a few hundred hydrogen atoms per cm^3 and gas kinetic temperatures, T, of approximately 100 K]. The interpretation of these pioneering hydride detections was not obvious. Early attempts to model the formation of CH and CH^+ focused on the slow radiative association of C^+ and C with hydrogen atoms (Kramers & Ter Haar 1946). Chemical reactions with H_2 (note that throughout the manuscript, we use the terms "H_2" and "molecular hydrogen" interchangeably) were ignored because they were known to be endothermic and because interstellar H_2 was not even detected. Bates & Spitzer (1951) suggested that molecules such as CH^+ could be a dissociation product of CH_4 sublimated from grains near stars. Both atomic and molecular hydrogen were discovered later in the cold neutral medium (CNM), HI at 1420 MHz by radio techniques in the 1950s (Ewen & Purcell 1951), and H_2 twenty years later by electronic absorption lines in the FUV from sounding rockets and from *Copernicus* satellite observations (e.g., Carruthers 1970, Spitzer et al. 1973).

Millimeter- and radio-frequency searches for rotational and Λ-type doubling emissions were also recognized as a promising method for detecting new interstellar molecules, for example by Townes (1957), who presented predictions for the frequencies of several key transitions. These early line frequency predictions contributed to the development of radio astronomy in the centimeter domain and led to the first detection of OH at 1.7 GHz (Weinreb et al. 1963), NH_3 at 23 GHz (the first polyatomic molecule in space; Cheung et al. 1968), and H_2O at 22 GHz (Cheung et al. 1969). OH was also the first molecule detected outside the Milky Way (Weliachew 1971). The team of Nobel Prize winner C.H. Townes made the discoveries of NH_3 and H_2O. Most of the subsequent discoveries of new molecules resulted from the development of higher-frequency heterodyne receivers in the millimeter and submillimeter domains accessible to ground-based telescopes, and more recent work has been enabled by observations in the FIR, a wavelength region that is only available from stratospheric and space observations (e.g., Gerin et al. 2012, and references therein). These techniques allow the detection of pure rotational transitions at very high spectral resolution (less than 1 km s^{-1}); thus fine and hyperfine line splittings can be resolved. In addition, the FIR domain allows the detection of rotationally excited emission lines. This permits high temperature and density environments ($T > 100$ K and $n_H > 10^4$ cm^{-3}), such as those in star-forming regions, to be probed. In diffuse and translucent clouds, hydrides such as CH^+, CH, HCl, NH, OH, OH^+ or SH can now be studied through their electronic absorption bands in the UV domain at velocity resolutions of a few km s^{-1} (e.g., Federman et al. 1995, Krełowski et al. 2010, Zhao et al. 2015). NH, in particular, was first detected in this domain (Meyer & Roth 1991). In dense but cold clouds ($T \simeq 20$ K), hydrides also exist in the solid phase as ice mantles covering dust grains (see the review by Boogert et al. 2015). Their vibrational modes can be detected in the IR domain. The first mantles detected in absorption were water and ammonia ices (Merrill et al. 1976). **Table 1** shows a compilation of the detected hydrides and the wavelength range in which they have been observed.

The formation of H_2 on grain surfaces rather than in the gas phase was soon established, and the first models suggested that most hydrogen should be molecular at visual extinctions $A_V > 1.5$ mag (e.g., Hollenbach et al. 1971). Watson & Salpeter (1972) proposed that other molecules formed on grains as well. More complete chemical models of diffuse clouds were developed (Solomon & Klemperer 1972, Black & Dalgarno 1977). Herbst & Klemperer (1973) modeled the chemistry

Cold neutral medium (CNM): two neutral phases coexist at pressure equilibrium in the ISM, the warm neutral medium with $T \sim 10^4$ K and $n_H \sim 0.3$–1 cm^{-3}, and the CNM with $T \sim 10^2$ K and $n_H \sim 30$–100 cm^{-3}

Far ultraviolet (FUV): the 91.2–200 nm wavelength region, corresponding to photon energies of 6–13.6 eV

Far infrared (FIR): the 20–300 μm wavelength region, corresponding to frequencies of 1–15 THz

Table 1 Main astrophysical hydrides[a]

Formula	Name	Spectral domain[b]	Reference
H_2	Molecular hydrogen	UV-visible, IR, FIR	Carruthers 1970
H_3^+	Protonated molecular hydrogen	IR	Geballe & Oka 1996
CH	Methylidyne	UV-visible, (sub)mm, cm	Swings & Rosenfeld 1937
CH_2	Methylene	FIR, (sub)mm	Hollis et al. 1995
CH_3	Methyl	IR	Feuchtgruber et al. 2000
CH_4	Methane	IR	Lacy et al. 1991
CH^+	Methylidynium	UV-visible, FIR, (sub)mm	Douglas & Herzberg 1941
CH_3^+	Methylium	IR, (sub)mm	Roueff et al. 2013[c]
NH	Imidogen	UV-visible, (sub)mm	Meyer & Roth 1991
NH_2	Amidogen	(sub)mm	van Dishoeck et al. 1993
NH_3	Ammonia	(sub)mm, cm	Cheung et al. 1968
NH_4^+	Ammonium	(sub)mm	Cernicharo et al. 2013[d]
OH	Hydroxyl radical	UV-visible, FIR, cm	Weinreb et al. 1963
H_2O	Water	FIR, (sub)mm, cm	Cheung et al. 1969
OH^+	Hydroxylium	UV-visible, (sub)mm	Wyrowski et al. 2010
H_2O^+	Oxidaniumyl	UV-visible, (sub)mm	Ossenkopf et al. 2010
H_3O^+	Hydronium	FIR, (sub)mm	Phillips et al. 1992
HF	Hydrogen fluoride	FIR	Neufeld et al. 1997
SH	Mercapto radical	UV-visible, FIR	Neufeld et al. 2012
H_2S	Hydrogen sulfide	(sub)mm	Thaddeus et al. 1972
SH^+	Sulfanylium	(sub)mm	Benz et al. 2010, Menten et al. 2011
HCl	Hydrogen chloride	UV-visible, (sub)mm	Blake et al. 1985
HCl^+	Chloroniumyl	FIR	De Luca et al. 2012
H_2Cl^+	Chloronium	(sub)mm	Lis et al. 2010a
ArH^+	Argonium	(sub)mm	Barlow et al. 2013

[a]Adapted from The Astrochymist (**www.astrochymist.org**).
[b]The corresponding wavelength ranges are: UV-visible, 100–1000 nm; IR, 1–20 μm; FIR, 20–300 μm; (sub)mm, 0.3–4 mm; cm, 1–20 cm.
[c]A tentative detection of the isotopologue CH_2D^+ is reported.
[d]The detection of the isotopologue NH_3D^+ is reported.

of molecular cloud interiors (where most hydrogen is in the form of H_2) and predicted it to be dominated by ion-molecule reactions maintained by cosmic ray (CR) particle ionization. These chemical models were the basis of more sophisticated diffuse cloud, dense photodissociation region (PDR), shock, and turbulent dissipation models developed later in the 1980s. Supported by laboratory and theoretical studies, these models were also critical in predicting the existence of new hydride molecules in space. Review articles have been presented previously by van Dishoeck (1998) and Snow & McCall (2006) on diffuse interstellar clouds, by Hollenbach & Tielens (1999) on PDRs, and by Bergin & Tafalla (2007) and Caselli & Ceccarelli (2012) on dark clouds.

Recent years have seen rapid progress in our understanding of interstellar hydrides, with new detections and modeling approaches demonstrating their diagnostic power. Thus it seems appropriate to review the current state of observations in different interstellar environments and the unique astrophysical information that can be obtained from them. This review is organized as follows. After a general introduction of the thermochemical properties and of the excitation of hydrides in Section 1, in Section 2 we summarize the main gas-phase and solid-phase processes driving the chemistry of hydrides. We then focus on the appearance of hydride molecules in

PDR: photodissociation region

diffuse molecular gas (Section 3), in dense and strongly UV-irradiated gas (Section 4), in shocks and turbulent dissipation regions (Section 5), and in cold and dense gas shielded from UV radiation (Section 6). In Section 7, we summarize the diagnostic power of hydrides, and in Section 8 we extend our discussion to external galaxies. We end by giving our conclusions and anticipating some of the exciting prospects for hydride research in the years to come.

1.2. Thermochemistry of Interstellar Hydrides

Although the interstellar gas is far from thermochemical equilibrium (TE), key features of the chemistry of interstellar hydrides—discussed in detail in Section 2—are determined by thermochemistry (Neufeld & Wolfire 2009). Among the elements in the second and third rows of the periodic table, F, O, N, Ne, and Ar (note that throughout this manuscript, we use the chemical symbols interchangeably with the spelled-out element names) all have first ionization potentials greater than that of atomic hydrogen (13.60 eV); because hydrogen atoms shield them very effectively from UV radiation of sufficient energy to ionize them, these elements are predominantly neutral in the CNM. All other elements in the second and third rows of the periodic table—including C, Si, P, S and Cl—have ionization potentials smaller than that of hydrogen; typically, they are predominantly singly-ionized in the cold diffuse ISM. (The exception is Cl, which may exhibit a significant neutral fraction in clouds with a sufficient H_2 fraction: This behavior is a consequence of the rapid reaction of Cl^+ with H_2 to form HCl^+, which subsequently undergoes dissociative recombination to form atomic Cl.)

With the notable exception of HF, every neutral diatomic hydride has a dissociation energy smaller than that of H_2, as indicated in **Figure 1**. As a result, hydrogen abstraction reactions of the type $X + H_2 \rightarrow XH + H$ are all endothermic except in the case where X is fluorine. HF is therefore the only neutral diatomic hydride that can be formed at low temperature through the reaction of an atom with H_2. As for the diatomic hydride cations, HeH^+, OH^+, HF^+, HCl^+, ArH^+ and NeH^+ have dissociation energies larger than that of H_2. They can, therefore, be produced

H_2 4.48							
LiH 2.41	BeH 2.24	BH 3.44	CH 3.49	NH 3.22	OH 4.39	HF 5.87	
NaH 2.04	MgH 1.99	AlH 2.95	SiH 2.98	PH 2.87	SH 3.65	HCl 4.43	
KH 1.87	CaH 1.77	GaH 2.78	GeH 2.73	AsH 2.66	SeH 3.11	HBr 3.76	

ScH 2.09	TiH 2.08	VH 1.67	CrH 2.27	MnH 1.27	FeH 1.59	CoH 1.97	NiH 2.57	CuH 2.64	ZnH 0.83

Figure 1

Dissociation energies of the neutral diatomic hydrides, in eV, from Neufeld & Wolfire (2009) and based upon the thermochemical data referenced therein. Adapted with permission from the AAS.

Element	Ionization potential (eV)	Endothermicity (Kelvin equivalent = $\Delta E/k_B$) for			Driver
		$X + H_2 \rightarrow XH + H$	$X^+ + H_2 \rightarrow XH^+ + H$	$X + H_3^+ \rightarrow XH^+ + H_2$	
He	24.587	No reaction	Exothermic, but primary channel is to He + H + H^+	29,000	
C	11.260	11,000	4,300 ☑		Warm gas
N	14.534	15,000	230	10,000	Cosmic rays
O	13.618	920 ☑	☑	☑	Warm gas or cosmic rays
F	17.423	☑		10,000	None needed
Ne	21.564	No reaction	Exothermic, but primary channel is to Ne + H + H^+	27,000	
Si	8.152	17,000	15,000		Warm gas
P	10.487	19,000	13,000		Warm gas
S	10.360	10,000	10,000 ☑		Warm gas
Cl	12.968	515	☑		UV with $h\nu > 12.97$ eV
Ar	15.760	No reaction	☑	6,400	Cosmic rays

Figure 2

Ionization potentials for selected elements, and endothermicities of three key reactions of possible importance in the formation of interstellar hydrides. Here, the endothermicities, ΔE, are presented as temperatures, $\Delta E/k_B$, and given in units of Kelvin. Cells shown in green indicate exothermic reactions, those shown in orange indicate slightly endothermic reactions with $\Delta E/k_B \leq 1000$ K, and those shown in red indicate endothermic reactions with $\Delta E/k_B \geq 1000$ K. Where the reactant (X or X^+) is the dominant ionization state of the element in diffuse interstellar gas clouds with a small molecular fraction, the green, orange, or red coloring is solid; otherwise, the cell is shaded. Check marks indicate reactions that have been invoked as significant production routes in astrochemical models in the literature. As indicated in **Table 1**, CH, CH^+, NH, OH, OH^+, HF, SH, SH^+, HCl, HCl^+, and ArH^+ have been detected in the ISM.

exothermically[1] via the hydrogen abstraction reaction $X^+ + H_2 \rightarrow XH^+ + H$; such reactions are endothermic for all other ions XH^+.

In addition to the ionization potential of each atom X and the dissociation energies of the hydrides XH and XH^+, another important thermochemical parameter is the proton affinity of X. Because H_3^+ is produced efficiently following CR ionization of H_2, proton transfer from H_3^+ can be an important production mechanism for XH^+ when the proton affinity of X exceeds that of H_2 (422.3 kJ mol^{-1}, or equivalently, 4.38 eV). This condition is satisfied for C, O, Si, P, S and Cl—but not for N, F, Ne or Ar—with the result that the first six atoms can react exothermically with H_3^+ to form XH^+. This consideration is most important for O, because it is the only atom among these six to be predominantly neutral in diffuse clouds.

In **Figure 2**, the thermochemical considerations discussed above are presented in graphical form. For each element, the first ionization potential is given in the second column from the left. The third, fourth, and fifth columns indicate the endothermicity of three key reactions: the reaction of X with H_2 to form XH, the reaction of X^+ with H_2 to form XH^+, and the reaction of

[1]For Ne^+ and He^+, the alternative reaction channel to $X + H + H^+$ is also exothermic and is favored.

X with H_3^+ to form XH^+. Particularly for neutral-neutral reactions, the activation energy (i.e., the energy barrier) may exceed the endothermicity. For example, the reaction of O with H_2 to form OH and H has an endothermicity $\Delta E/k_B \sim 920$ K but an activation energy of $\Delta E_A/k_B \sim 3000$ K. The dominant production mechanisms for diatomic interstellar hydrides, and the environments in which they are found, can largely be inferred from the information presented in this matrix. In some cases, different mechanisms are important in different environments: In the case of oxygen, for example, production of OH via the endothermic reaction of O and H_2 becomes rapid in warm ($T \geq 400$ K) gas (e.g., Kaufman & Neufeld 1996), whereas OH^+ production is effective in cold diffuse gas through reaction of O^+ with H_2 or (in slightly denser gas with a larger H_2 fraction) of O with H_3^+ (e.g., Hollenbach et al. 2012).

Local thermodynamic equilibrium (LTE): the state in which the level populations of a given molecule are determined by Boltzmann equilibrium at the local kinetic temperature T

Critical density: the density at which the rate of collisional deexcitation from a given state is equal to the rate of spontaneous radiative decay

1.3. Excitation of Interstellar Hydrides

Several physical processes determine the excitation of interstellar hydrides (e.g., Roueff & Lique 2013, and references therein), including collisional excitation, spontaneous radiative decay, radiative excitation, and formation pumping. At sufficiently high densities, the first of these processes drives the molecular excitation to local thermodynamic equilibrium (LTE), in which the relative level populations are given by Boltzmann factors determined by the gas kinetic temperature. However, the critical density needed to achieve LTE is typically larger for the rotational states of hydrides than that for those of nonhydride interstellar molecules, because hydrides have smaller momenta of inertia, larger rotational constants, and much larger spontaneous radiative rates (scaling as the cube of the transition frequency for a given dipole matrix element). At densities below the critical density, the level populations reach a quasi-equilibrium in which the total production and loss rates are equal for every state. In general, the excitation is subthermal, with the excitation temperatures for most transitions being smaller than the gas kinetic temperature. However, specific transitions can sometimes be suprathermally excited, or even inverted, giving rise to maser amplification.

In diffuse molecular clouds, the molecular excitation is often determined primarily by the radiation field; in clouds that are not close to a strong submillimeter radiation source, the cosmic microwave background radiation (CMB) dominates and most rotational transitions have an excitation temperature close to that of the CMB. For molecules such as HF and HCl, in which there are no metastable rotational states, this means that most molecules are found in the ground rotational state. For triatomic hydrides such as H_2O, H_2O^+, and H_2Cl^+, in which there are two spin symmetries (*ortho* with total H nuclear spin 1, and *para* with total H nuclear spin 0), most molecules in diffuse clouds are found in either one or the other of the lowest rotational states of the two spin symmetries. For symmetric top molecules such as NH_3 and H_3O^+, in which the rotation is characterized by the quantum numbers J and K, the lowest energy state for any given K is metastable. Thus, for NH_3 and H_3O^+ in diffuse clouds, the population is largely divided among those metastable states lying at the bottom of each K-ladder.

Although the CMB radiation is ubiquitous, other radiation fields can become important in specific environments: Strong mid-IR and FIR radiation is present close to massive protostars, for example, and strong optical and UV radiation is present close to hot stars. Such radiation may affect the rotational populations in the ground vibrational state as a result of pumping through rotational (FIR), vibrational (mid-IR), and electronic (optical and UV) transitions (Godard & Cernicharo 2013).

In different astrophysical environments, inelastic collisions with H_2, H, and/or electrons can be important or even dominant in determining the equilibrium populations in the various rovibrational states of an interstellar hydride. Collisions with He can also be important but probably never

play a dominant role. In dense, well-shielded molecular clouds, H_2 is the most important collision partner, but in PDRs where the carbon is significantly photoionized, excitation by electrons can be important or dominant. Although the electron abundance relative to H_2 in such regions is only a few $\times 10^{-4}$, the rate coefficients for electron impact excitation can exceed those for excitation by H_2 or H by four orders of magnitude, particularly in the case of hydride cations or neutral hydrides with large dipole moments: Here, the cross sections are enhanced by long-range Coulomb interactions (and the mean electron velocities exceed the mean H_2 velocities by the square root of the H_2-to-electron-mass ratio). In certain environments, particularly the molecule reformation region behind dissociative shock fronts (see Section 5 below), excitation by atomic hydrogen can also be very important.

There is a considerable and ongoing effort to calculate state-to-state rate coefficients for various hydrides of astrophysical interest, most importantly in recent years for the excitation of water by *ortho*- and *para*-H_2 (Daniel et al. 2011 and references therein) and by atomic hydrogen (Daniel et al. 2015). State-of-the-art quantal calculations make use of the so-called close-coupling method and rely upon accurate determinations of the potential energy surface for the system. Such calculations are computationally expensive and are often (e.g., in the case of water) limited to a subset of the rovibrational states that have actually been observed in interstellar hydrides. As a result, less computationally intensive (and less accurate) methods such as quasi-classical trajectory calculations (e.g., Faure et al. 2007) must sometimes be used to interpret astronomical observations, in some cases accompanied by extrapolation methods involving propensity rules (e.g., Faure et al. 2007) or the use of artificial neural networks (Neufeld 2010). The Leiden Atomic and Molecular Database (Schöier et al. 2005) and BASECOL (Dubernet et al. 2013) databases have been established to collate collisional rate coefficients and spontaneous radiative decay rates for hydrides and other interstellar molecules in a standard format for use in modeling the excitation.

Formation pumping is another process that can affect the excitation state of interstellar hydrides. Here, if the lifetime of the molecule is comparable to—or smaller than—the timescale on which the quasi-equilibrium level populations are established, the observed populations may reflect the initial conditions at formation. The most clearly established case of formation pumping in interstellar hydrides is the excitation of high-lying OH rotational states following the photodissociation of H_2O to form OH (Tappe et al. 2008; discussed further in Section 5). Formation pumping has also been discussed as an explanation for the observed excitation of H_3O^+ (e.g., González-Alfonso et al. 2013, Lis et al. 2014) and may be important for other molecular ions as described in Section 4.

2. CHEMISTRY

2.1. Gas-Phase Processes

As mentioned in Section 1.2, hydrides in the gas are mostly formed through a series of hydrogen abstraction reactions combined with dissociative recombination. The chemistry of C, O, and N hydrides is illustrated in **Figure 3**. This relative simplicity hides subtleties introduced by (*a*) the presence of highly endothermic reactions on important pathways (e.g., the initiation reaction of the carbon chemistry between ionized carbon and molecular hydrogen has an endothermicity of 0.37 eV, or 4300 K), and (*b*) the dependence of the reaction rates and products on the molecular hydrogen spin symmetry state, or more generally on the initial rovibrational state (for molecules) or the fine structure level (for atoms) of the reactants (e.g., Faure et al. 2013, Li et al. 2013). Fortunately, many of the key reactions for hydride synthesis have been studied through theoretical calculations and laboratory measurements because of their fundamental interest for molecular

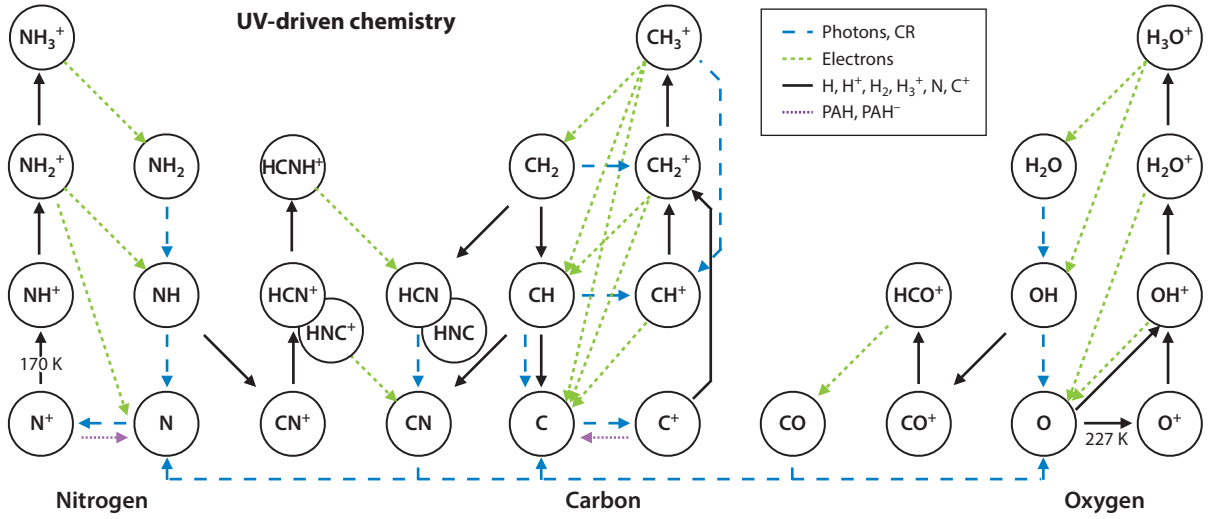

Figure 3

Illustration of the chemical network initiating the carbon, oxygen, and nitrogen chemistry in diffuse cloud conditions ($n_H = 50$ cm^3, $A_V = 0.4$ mag, $\chi = 1$). The black arrows show the reactions with H, H^+, H_2, H_3^+, C^+, and N, with values of the endothermicity for the reaction between N^+ and H_2 and for the charge exchange reaction between O and H^+. Note that CH_2^+ is formed in the slow radiative association reaction between C^+ and H_2. The dashed blue arrows indicate the reactions induced by FUV photons or cosmic rays (CR). Dissociative recombination reactions with electrons are shown with green dotted arrows. Purple arrows show the neutralization reactions on dust grains and polycyclic aromatic hydrocarbons (PAHs). Adapted from Godard et al. (2014) with permission.

physics. For example, the neutral-neutral reaction between F and H_2 forming HF and H is one of the benchmark systems for the tunneling effect. Combining measurements down to 11 K and new theoretical calculations, Tizniti et al. (2014) have provided an accurate determination of this important reaction rate.

The hydrogen abstraction reactions initiating the O, N, Cl, and Ar chemistry are exothermic or moderately endothermic (for N). Because dissociative recombination reactions are fast, photodissociation is usually not a dominant destruction process for the hydride ions, but it affects neutral hydrides. The hydride chemistry is sensitive to the strength and spectrum of the incident X-ray and UV radiation field, and to the ionization rate due to CRs, the two main sources of ionization. The exact energy distribution of the UV field is particularly important for the Cl chemistry because the ionization potential of atomic Cl, 12.968 eV, is very close to the Lyman edge (13.6 eV). Polycyclic aromatic hydrocarbons (PAHs) play a role in the chemistry because cations (e.g., H^+, C^+, and N^+) get neutralized when encountering a neutral or negatively charged PAH. Hence PAHs reduce the efficiency of molecule formation. This is especially important for the oxygen chemistry in which the initiating charge exchange reaction between H^+ and O competes with neutralization on PAHs.

Given the relatively large reaction rates, the chemical timescales for gas-phase hydride production are short, typically less than a few × 100 yr provided that molecular hydrogen has reached its equilibrium abundance. The formation of molecular hydrogen itself, which occurs on grain surfaces, is significantly slower, with typical timescales of 10 Myr for diffuse gas densities. Numerical simulations of the diffuse ISM, using either hydrodynamic or magnetohydrodynamic (MHD) codes, have shown however that the equilibrium molecular hydrogen fraction can be reached faster in a dynamical medium because the compressions induce transient density enhancements, where

Cosmic rays (CRs): energetic particles (electrons, protons, and heavier nuclei), accelerated at energies between 0.1 and 10^6 GeV in fast shocks

Polycyclic aromatic hydrocarbons (PAHs): carbon and hydrogen molecules composed of multiple benzenic cycles with hydrogen atoms at the boundaries

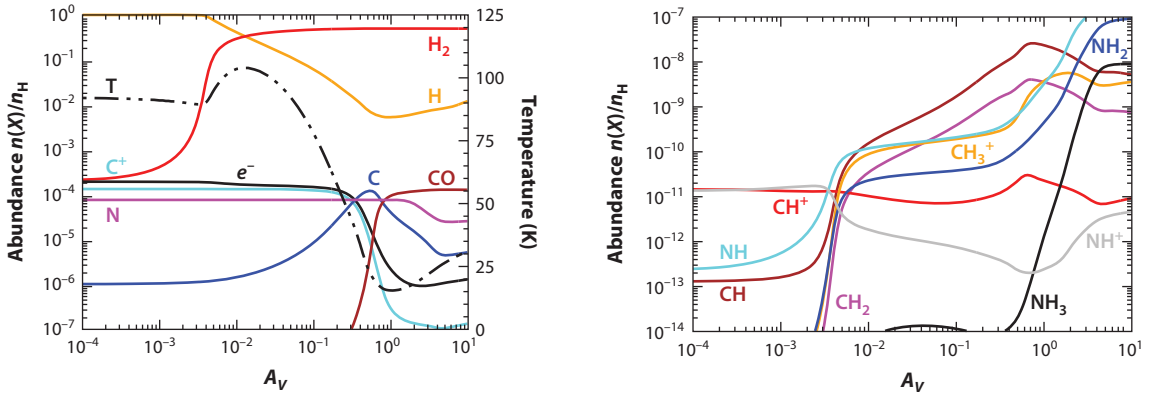

Figure 4

Variation of the gas-phase abundances of various species relative to the total hydrogen content as a function of depth A_V for a cloud with constant pressure $P/k_B = 4 \times 10^3$ K cm^{-3}, irradiated by the average interstellar radiation field ($\chi = 1$) from the left side, and a cosmic-ray ionization rate $\zeta_H = 2 \times 10^{-16}$ s^{-1}, computed with the Meudon photodissociation region code (Le Bourlot et al. 2012). (*Left*) The hydrogen (H, H_2), carbon (C^+, C, CO), and nitrogen (N, N_2 not shown) reservoirs together with the electron abundance and the kinetic temperature (*right vertical scale*). The gas density ranges from approximately 40 cm^{-3} at $A_V \sim 0.01$ mag up to ~150 cm^{-3} at $A_V > 1$ mag. (*Right*) The main carbon and nitrogen hydride abundances as a function of extinction.

H_2 forms more rapidly than in an uniform medium (Glover & Mac Low 2007). The timescale for conversion between the H_2 spin symmetry states strongly depends on whether only gas-phase processes contribute, or whether H_2 is rapidly thermalized on dust grains (Le Bourlot 2000). In the former case, the conversion is slow, with a similar timescale as the static formation rate of H_2 (e.g., Pagani et al. 2011). Conversion on grain surfaces is expected to be faster, but a small fraction of *o*-H_2 (~10^{-3}) is expected to remain even at low temperatures because of the presence of newly formed H_2 molecules, either on grains or through chemical reactions (Le Bourlot 2000). Several hydrides (e.g., NH_3, NH_2, or H_2O) exhibit spin symmetry states whose relative abundances are sensitive to the H_2 *ortho*-to-*para* ratio (OPR) in the gas.

State-of-the-art chemical models accurately predict (within better than a factor of two) the observed abundances of most of the abundant hydrides, and their respective relationships. **Figure 4** illustrates the behavior of carbon and nitrogen hydrides for a cloud with constant pressure $P/k_B = 4 \times 10^3$ K cm^{-3} using a pure gas-phase chemical network (except for H_2). The behavior of oxygen hydrides is illustrated in the left panel of **Figure 5**, which displays a model with a similar value of the control parameter χ/n_H, where χ represents the enhancement factor of the incident FUV radiation field over the mean interstellar radiation field in the solar neighborhood. Interestingly, CH and CH_2 show a very similar behavior with a first rise of their relative abundances nearly coinciding with the H/H_2 transition at $A_V \sim 0.1$ for this particular model. The appearance of nitrogen hydrides (NH, NH_2 and NH_3) takes place further inside the cloud at $A_V \sim 1$ and coincides with the CO formation zone. The NH^+ abundance remains low, in agreement with *Herschel* observations (Persson et al. 2012). The series of molecular ions OH^+, H_2O^+, and H_3O^+ behaves somewhat differently from the carbon and nitrogen hydrides: each ion is predicted to probe a different zone of molecular hydrogen content, with $f_{H_2} = 2n(H_2)/[2n(H_2) + n(H)]$, the molecular fraction, increasing from OH^+ to H_3O^+. As we discuss further in Section 7, this property is fully consistent with observations and can be used to derive the fraction of molecular hydrogen in the region of maximum OH^+ abundance.

***Ortho*-to-*para* ratio (OPR):** the ratio between the densities, or column densities, of the *ortho* and *para* nuclear spin symmetry states

***The Herschel Space Observatory* (*Herschel*):** a FIR and submillimeter satellite observatory (55–672 μm) with a 3.5 m primary mirror, operated by ESA from 2009–2013 with important participation from NASA

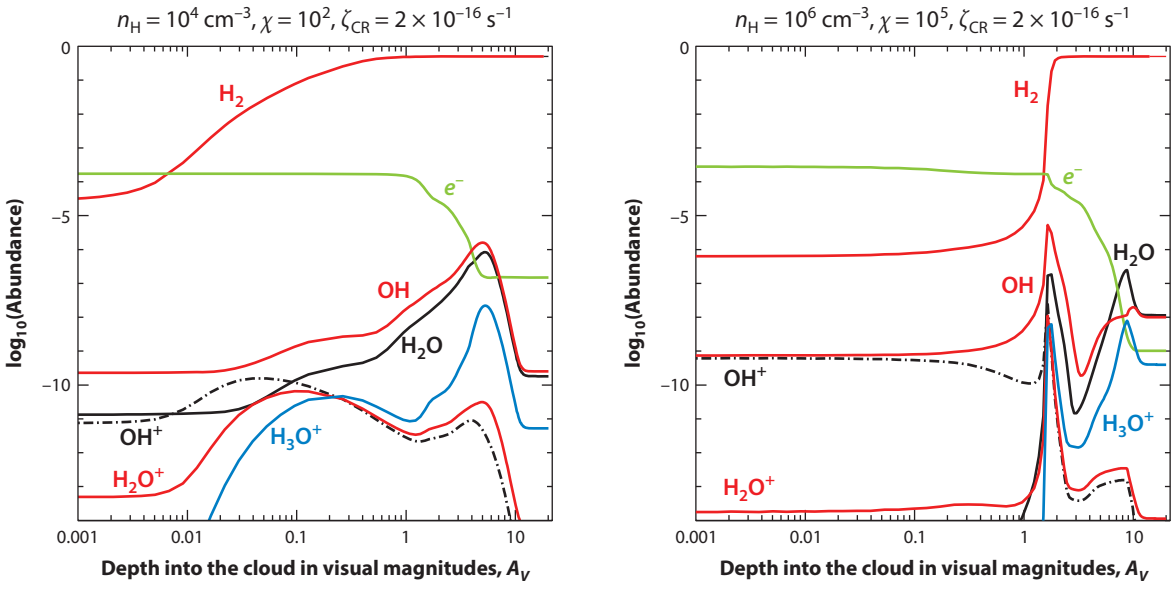

Figure 5

Predicted gas-phase abundances of several hydrides with respect to H nuclei as a function of depth A_V into the cloud, for photodissociation regions with (*left*) $n_H = 10^4$ cm^{-3}, $\chi = 10^2$, and $\zeta_{CR} = 2 \times 10^{-16}$ s^{-1}, and (*right*) with $n_H = 10^6$ cm^{-3} and $\chi = 10^5$. Adapted from Hollenbach et al. (2012) with permission from the AAS.

2.2. Solid-Phase Processes

Molecular hydrogen is not the only molecule formed in the solid phase. Recent studies have shown that even under diffuse ISM conditions, the formation of molecules on grain surfaces can be efficient (see, e.g., Sonnentrucker et al. 2015 for H_2O). Hydrides are particularly susceptible to being formed on grain surfaces because of the ubiquitous presence of hydrogen. Laboratory experiments using beams of hydrogen and oxygen atoms hitting a cold surface have clearly demonstrated that water ice forms in this process. A fraction of the newly formed molecules does not stay on the cold surface but is immediately released in the gas phase (Dulieu et al. 2013), a process called chemical desorption. The fractions of trapped versus ejected molecules depend on the nature of the surface, the ice coverage, and the exact reaction mechanism. In a similar manner to water ice, the hydrogenation of carbon and nitrogen atoms produces methane and ammonia. Laboratory experiments are now able to probe these processes, including exchanges between H and D atoms and the production of deuterated species (Fedoseev et al. 2015).

Once formed on the cold grain surfaces, four mechanisms may release molecules to the gas phase: (*a*) thermal sublimation when the grains reach temperatures larger than the ice sublimation threshold, (*b*) photodesorption when FUV photons are absorbed by the grain surface and kick some molecules out of the ice, (*c*) CR-induced desorption when an energetic particle interacts with a grain mantle, and (*d*) chemical desorption during the formation process. Laboratory experiments have been performed to study these mechanisms and understand in which conditions they operate. Theoretical and laboratory studies of ice photodesorption have concluded that this process is complex. FUV photons can dissociate a frozen water molecule, producing two fragments (H and OH) that have excess energy. Either these fragments can recombine as a gas-phase water molecule, or the excited H can kick out another frozen water molecule. The outcome depends

on many parameters, but the most important is where the FUV photon is absorbed, because only the upper ice layers participate in the desorption process. The presence of isotopologues of other molecules such as CO, which does not dissociate upon the absorption of a FUV photon, will also affect the desorption yield. Overall, the photodesorption yields range between 10^{-4} and 10^{-2} molecules/photon (Arasa et al. 2015). With such numbers, most of the species are predicted to be frozen in dense core conditions, with a minor fraction remaining in the gas phase. As illustrated in **Figure 5**, water vapor reaches its peak abundance for extinctions of a few magnitudes. Chemical models also include a temporal dimension because the dynamical timescales, which scale with the free-fall time $t_{\rm ff} = \sqrt{3\pi/32{\rm G}\rho} \sim 10^5\sqrt{5 \times 10^4\,{\rm cm}^{-3}/n({\rm H}_2)}$ yr, are similar to the chemical timescales. For instance, the freeze-out timescale in the absence of desorption is $t_{\rm freeze} \sim 10^5[10^4\,{\rm cm}^{-3}/n({\rm H}_2)]$ years.

Although the respective abundances of H_2O, CH_4 and NH_3 are fairly well documented in interstellar ices, little is known about the presence of hydrides composed of the heavier elements F, S, and Cl in ices. The somewhat lower elemental abundances preclude a direct identification given the limited sensitivity of IR spectroscopy of solid features—the weakest solid-state features detected through IR spectroscopy correspond to column densities of about 1% that of water ice. Solid-phase and gas-phase processes are coupled, as shown, for instance, by the production of H_2 and methane during the FUV irradiation of hydrogenated amorphous carbons (Alata et al. 2014). Although laboratory experiments have led to steady progress in the understanding of the solid-phase chemistry, the state of the art is still far from that of the chemistry in the gas phase, even for simple hydrides. The relative contributions of solid-phase and gas-phase routes to the formation of nitrogen hydrides deserve specific attention. Although the reaction between N^+ and H_2 initiates the nitrogen chemistry in UV-illuminated regions, NH is mostly formed as a minor channel in the dissociative recombination of N_2H^+ in shielded regions. As discussed by Wagenblast et al. (1993), the gas-phase production route for nitrogen hydrides is not efficient enough to explain the observed abundance in diffuse clouds, especially if the CR ionization rate is low. An alternative formation mechanism for nitrogen hydrides involves the hydrogenation of nitrogen atoms on grain surfaces to form ammonia, and its release into the gas phase for further processing. Given the wealth of data now available, the relative contributions of solid-phase and gas-phase routes in the nitrogen chemistry should be assessed, especially for diffuse conditions. More generally, to improve astrophysical models, more quantitative evaluations of the reactivity of atoms and molecules (including diffusion) and the efficiency of the various desorption processes are needed.

3. HYDRIDES IN DIFFUSE GAS

3.1. Overview

With the exception of CH_4, CH_3^+ and NH_4^+, all the hydride molecules listed in **Table 1** are known to be present in diffuse molecular clouds. Observations of hydrides in diffuse clouds have targeted transitions over a wide range of wavelengths, from a 122-nm electronic transition (of OH) to a set of 18-cm Λ-doubling transitions (also of OH). Typically, molecules in diffuse clouds have been observed in absorption toward background sources of continuum radiation; these include hot stars (at UV wavelengths), warm dust in regions of active star formation (at FIR and submillimeter wavelengths), and HII regions (at centimeter wavelengths). With the exception of those targeting centimeter-wavelength Λ-doubling transitions, absorption-line observations yield relatively robust and model-independent estimates of molecular column densities. This advantage results from the fact—discussed previously in Section 1.3—that under typical conditions in diffuse

clouds, most hydride molecules are found primarily in the ground state (or, for triatomic hydrides, in the lowest energy states of the *ortho* and *para* symmetry states); thus, stimulated emission is typically negligible, and the scaling between absorption line optical depth and molecular column density is only weakly dependent upon the physical conditions. In the remainder of this section, we review the observational data on hydride molecules in diffuse clouds. In Section 7, we discuss how the measured abundances of interstellar hydrides can be used as quantitative probes of the environment in which they are found.

Stratospheric Observatory for Infrared Astronomy (SOFIA): an airborne 2.7 m telescope covering the wavelength range 1–655 μm, operated by NASA and the German Aerospace Center

3.2. Optical/UV and Centimeter-Wavelength Observations of Interstellar Hydrides

In diffuse molecular clouds, several hydride molecules show observable absorption at optical and UV wavelengths through their electronic transitions. These include three molecules—CH, CH^+, and NH—that were first detected (see **Table 1**) in this spectral region; two molecules—OH^+ (Krełowski et al. 2010) and SH (Zhao et al. 2015)—with optical/UV transitions that were detected shortly after their initial discovery at submillimeter wavelengths; as well as OH, detected both at UV (e.g., Snow 1976) and NUV wavelengths (e.g., Porras et al. 2014). In this spectral region, spectral resolving powers $R = \lambda/\Delta\lambda$ in excess of $\sim 10^5$ can be achieved with echelle spectrometers. Although these spectral resolving powers are not as high as those achievable at submillimeter wavelengths using heterodyne receivers, they nonetheless yield valuable kinematic information about the absorbing molecules. For example, a recent analysis of NUV spectra showing OH^+, OH, CH, CH^+, and CN absorption (Porras et al. 2014) has revealed a kinematic association between OH^+, CH^+, and neutral atoms on the one hand, and CN and OH on the other hand. CH is associated with both families, but the largest CH column densities usually occur in gas with a high molecular fraction. Because of the effects of dust extinction, optical/UV observations of absorption by molecules in the Galactic disk are limited to relatively nearby material, in contrast to the case of the submillimeter observations described in Section 3.3. At centimeter wavelengths, two hydride molecules—OH (e.g., Allen et al. 2015, and references therein) and CH (e.g., Chastain et al. 2010)—have been widely observed in diffuse interstellar gas clouds by means of their Λ-doubling transitions at 18 cm and 9 cm, respectively. Such transitions, which are typically observed in emission, have provided a valuable tracer of molecular hydrogen, as discussed in Section 7.

3.3. FIR and Submillimeter Observations of Absorption by Interstellar Hydrides

Over the past five years, *Herschel* and SOFIA (the Stratospheric Observatory for Infrared Astronomy) have provided unique opportunities to observe submillimeter absorption by many interstellar hydrides in diffuse clouds along the sight lines to bright submillimeter continuum sources. Heterodyne spectrometers available on both these observatories—the HIFI (Heterodyne Instrument for the Far-Infrared) instrument on *Herschel* and the GREAT (German Receiver for Astronomy at Terahertz Frequencies) instrument on SOFIA—have provided extremely high (<1 km s^{-1}) spectral resolution that is unmatched by other spectrometric techniques operating at submillimeter, IR, or visible wavelengths. *Herschel* observations have led to the discovery of interstellar SH^+, HCl^+, H_2Cl^+, H_2O^+ and ArH^+, and the first extensive observations of HF and OH^+; SOFIA observations have enabled the first detection of interstellar SH and have provided the first heterodyne observations of the 2.5 THz ground-state rotational line of OH.

Submillimeter absorption-line studies with *Herschel* and SOFIA have typically used strong continuum sources in the Galactic plane at distances up to ∼11 kpc from the Sun and with sight lines that can intersect multiple diffuse clouds in foreground spiral arms. Thanks to the differential

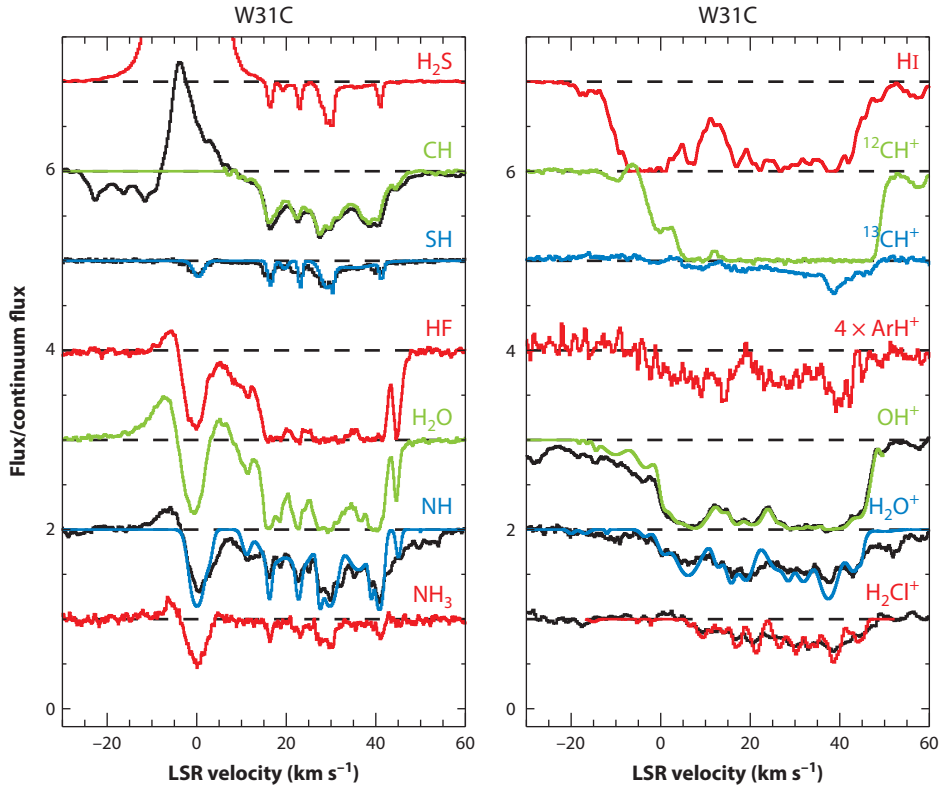

Figure 6

Absorption spectra observed toward W31C. (*Left*, *from top to bottom*) Spectra of H_2S $1_{10}-1_{01}$ at 168.8 GHz (based on data published by Neufeld et al. 2015a); CH $^2\Pi_{3/2}$ $J = 3/2-{}^2\Pi_{1/2}$ $J = 1/2$ at 532.7/536.8 GHz (Gerin et al. 2010a); SH $^2\Pi_{3/2}J = 5/2-3/2$ at 1381 GHz (Neufeld et al. 2015a); HF $J = 1-0$ at 1232 GHz; H_2O $1_{11}-0_{00}$ at 1113 GHz (Neufeld et al. 2010); NH $J_N = 2_1-1_0$ at 974.5 GHz; NH_3 $J_K = 2_1-1_1$ at 1215.2 GHz (Persson et al. 2010). (*Right*, *from top to bottom*) HI 21 cm (B. Winkel, manuscript in preparation); $^{12}CH^+$ $J = 1-0$ at 835.1 GHz (Godard et al. 2012); $^{13}CH^+$ $J = 1-0$ at 830.2 GHz (Godard et al. 2012); ArH^+ $J = 1-0$ at 617.5 GHz (Schilke et al. 2014); OH^+ $^2\Pi_{3/2}J = 5/2-3/2$ at 971.8 GHz (Gerin et al. 2010b); H_2O^+ $1_{11}-0_{00}$ at 1115 GHz (Gerin et al. 2010b); H_2Cl^+ $1_{11}-0_{00}$ at 485.4 GHz (Neufeld et al. 2012). For species with a partially resolved hyperfine splitting (CH, SH, NH, OH^+, H_2O^+), black lines show the observations and colored lines show the hyperfine-deconvolved spectra. For clarity, the spectra are separated by vertical offsets. The ArH^+ spectrum is expanded by a factor of 4 (in addition to being translated) so that the relatively weak absorption is clearer. Abbreviation: LSR, local standard of rest.

rotation of the Galaxy, different diffuse clouds along a single sight line give rise to separate velocity components in the observed absorption spectra. *Herschel* observations have been performed toward ~20 such continuum sources, revealing ~100 distinct components in which molecular column densities can be determined.

Figure 6 shows the spectra of a dozen hydride molecules observed along the sight line to W31C, a region of high-mass star formation located 4.95 kpc from the Sun, along with the HI 21 cm absorption line. All the spectra shown in **Figure 6** show clear evidence for absorption by foreground material in diffuse clouds along the sight line. For some molecules (e.g., SH and

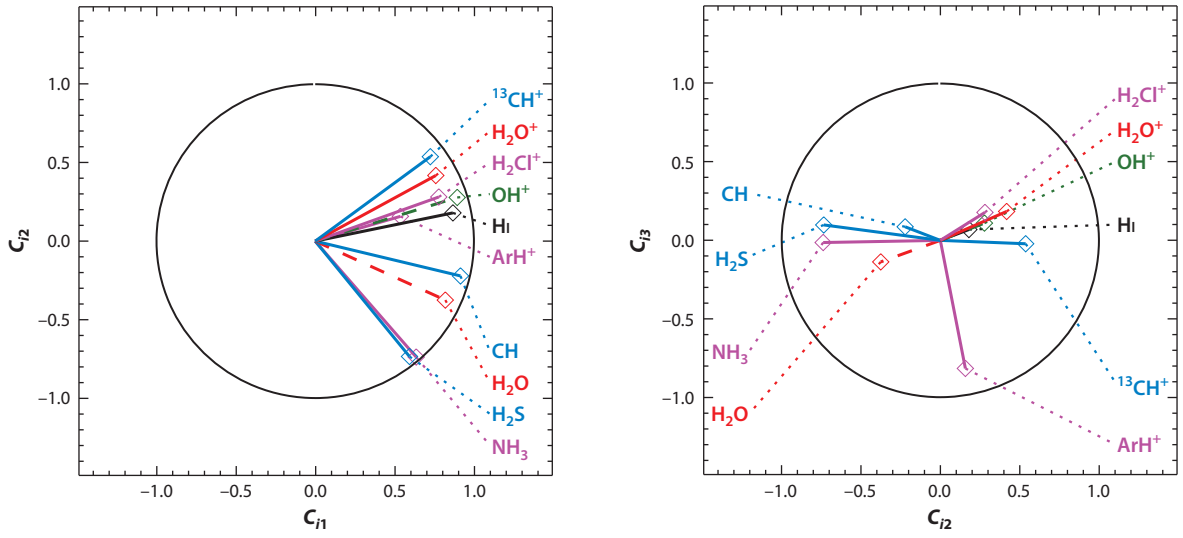

Figure 7

Results of principal component analysis for various species observed toward W31C. Diamonds indicate the coefficients obtained for each species in the (*left*) C_{i1}–C_{i2} and (*right*) C_{i2}–C_{i3} planes, and solid lines connect the origin to each diamond. In the limit where the first two principal components account for most of the variation in the spectra, the diamonds in the left panel lie on the unit circle, as explained by Neufeld et al. (2015b); moreover, the angle between the lines corresponding to any pair of species in that limit is equal to the arccosine of their correlation coefficient. Adapted from Neufeld et al. (2015b) with permission.

H_2S), the observed absorption is concentrated into five or six narrow features with line widths $\sim$1–3 km s^{-1}; other molecules—including most of the molecular ions—show a more extended distribution in velocity space and are less strongly concentrated into narrow absorption components. Neufeld et al. (2015b) have presented a more quantitative examination of the similarities and differences between these absorption spectra with the use of principal component analysis (PCA). Here, each optical depth spectrum (i.e., the plot of optical depth against velocity) is represented as a linear combination of a set of orthogonal (i.e., uncorrelated) eigenfunctions S_j chosen such that the first eigenfunction contains as much of the variation as possible, the second eigenfunction contains as much of the remaining variation as possible, and so forth. Typically, the species-specific spectrum i may be represented by a linear combination of the first two or three eigenfunctions, $C_{i1}S_1 + C_{i2}S_2$ ($+C_{i3}S_3$), which provides an excellent fit to the observed optical depth spectra, and the coefficients within that linear combination—C_{i1}, C_{i2}, and C_{i3}—can be used to describe the distribution of each absorbing species. **Figure 7** shows the first three coefficients obtained from a joint analysis of ten species along the W31C sight lines. The PCA results confirm that most of the molecular ions show a common distribution similar to that of HI, whereas most neutral species—particularly NH_3 and H_2S—tend to follow a distribution that is uncorrelated with HI. The ArH^+ molecular ion appears largely uncorrelated both with the other molecular ions and with the neutral molecules.

In **Table 2**, we summarize the typical hydride abundances derived for the diffuse ISM. In the case of molecular ions (with the exception of H_3O^+), these are shown relative to atomic hydrogen, whereas for neutral molecules, they are shown relative to H_2. In both cases, the corresponding abundances are also given relative to the gas-phase abundance of the relevant heavy element. The values shown in **Table 2** indicate that most hydride molecules in diffuse gas are only minor

Table 2 Typical hydride abundances in diffuse clouds

Molecule	Average abundance relative to H or H_2	Average abundance (fraction of gas phase elemental[a])	Method[b,c,d]	Reference for hydride column densities
CH	3.5×10^{-8}	1.3×10^{-4}	V, UV, M	Sheffer et al. 2008
CH_2	1.6×10^{-8}	6×10^{-5}	S, CH, M	Polehampton et al. 2005
CH^+	6×10^{-9}	4×10^{-5}	V, Re, M	Gredel 1997, Crane et al. 1995
CH_3^+	$<2 \times 10^{-9}$	$<1.4 \times 10^{-5}$	Re, V	Indriolo et al. 2010
NH	8×10^{-9}	6×10^{-5}	S, CH, 1	Persson et al. 2010
NH_2	4×10^{-9}	3×10^{-5}	S, CH, 1	Persson et al. 2010
NH_3	4×10^{-9}	3×10^{-5}	S, CH, 1	Persson et al. 2010
NH^+	$<4 \times 10^{-10}$	$<6 \times 10^{-6}$	S, HI, 1	Persson et al. 2010
OH	1×10^{-7}	1.6×10^{-4}	V, S, CH, M	Wiesemeyer et al. 2016, Lucas & Liszt 1996
H_2O	2.4×10^{-8}	4×10^{-5}	S, CH, M	Flagey et al. 2013
OH^+	1.2×10^{-8}	4×10^{-5}	S, HI, M	Indriolo et al. 2015
H_2O^+	2×10^{-9}	6.5×10^{-6}	S, HI, M	Indriolo et al. 2015
H_3O^+	2.5×10^{-9}	4×10^{-6}	S, CH, 1	Lis et al. 2014
HF	1.4×10^{-8}	0.4	S, CH, M	Sonnentrucker et al. 2010
SH	1.1×10^{-8}	4×10^{-4}	S, CH, M	Neufeld et al. 2015b
H_2S	5×10^{-9}	1.8×10^{-4}	S, CH, M	Neufeld et al. 2015b
SH^+	1.1×10^{-8}	8×10^{-4}	S, HI, M	Godard et al. 2012
HCl	1.5×10^{-9}	0.004	S, CH, 1	Monje et al. 2013
HCl^+	8×10^{-9}	0.04	S, CH, M	De Luca et al. 2012
H_2Cl^+	3×10^{-9}	0.02	S, CH, M	Neufeld et al. 2015a
ArH^+	3×10^{-10}	1×10^{-4}	S, HI, M[e]	Schilke et al. 2014

[a]Assuming the following gas-phase elemental abundances relative to hydrogen in the diffuse ISM: $C = 1.4 \times 10^{-4}$, $O = 3.1 \times 10^{-4}$, $N = 6.8 \times 10^{-5}$, $F = 1.8 \times 10^{-8}$, $S = 1.4 \times 10^{-5}$, $Cl = 1.8 \times 10^{-7}$, $Ar = 3.2 \times 10^{-6}$.

[b]Method for determination of hydride column density: V, visible or infrared observations of nearby stars; S, submillimeter, FIR (CH_2), or millimeter (H_2S) wavelength observations. Abundances determined from visible observations refer to the solar neighborhood, whereas abundances determined from (sub)millimeter and FIR observations also probe the Galactic plane halfway between the Galactic Center and the solar circle.

[c]Method for determination of H_2 or atomic hydrogen column density: UV, UV observations of H_2 Lyman and Werner bands; Re, reddening of background star; CH, submillimeter observations of CH with an assumed $N(CH)/N(H_2)$ ratio of 3.5×10^{-8}; HI, H 21-cm absorption line observations.

[d]Sample size: M, average (median) over multiple sources; 1, average (mean) over line of sight to W31C.

[e]Median value excludes clouds in the Galactic Center, where the abundances are typically an order of magnitude higher.

reservoirs of the heavy element they contain, with most heavy elements remaining overwhelmingly in atomic or singly-ionized form. The notable exception is HF, which, in diffuse regions with a large molecular hydrogen fraction, can account for most of the gas-phase fluorine. Chlorine is another element with a fairly strong tendency toward hydride formation; in clouds with a modest H_2 fraction, H_2Cl^+ can account for several percent of the gas-phase chlorine abundance. These behaviors are thought to reflect the thermochemical considerations summarized in **Figure 2**; fluorine and chlorine are the only elements that can react exothermically with H_2 when in their dominant stage of ionization (i.e., F and Cl^+) in diffuse clouds.

4. HYDRIDES IN DENSE, STRONGLY UV-IRRADIATED GAS

Although many aspects of diffuse molecular clouds can be understood in the framework of low-A_V, low-FUV field PDR models (for a review see Hollenbach & Tielens 1999), in this section

we focus on the presence of hydrides in more strongly UV-irradiated ($\chi > 10^3$ times the average interstellar radiation field), and denser gas ($n_H > 10^4$ cm^{-3}). These are conditions typical of the surface of dense molecular clouds illuminated by nearby massive stars, and also of the outer layers of irradiated protoplanetary disks (e.g., proplyds). Such dense PDRs are regulated by the presence of stellar FUV photons up to several magnitudes of extinction (i.e., high A_V). UV photons with energies higher than 13.6 eV ionize hydrogen atoms but they are absorbed in the adjacent HII regions. FUV photons, however, do dissociate molecules and ionize molecules and atoms with ionization potentials below 13.6 eV (C, S, Si, Na, Fe, etc.). Therefore, like diffuse clouds, dense PDRs are predominantly neutral, with maximum ionization fractions of $n_e/n_H \simeq 10^{-4}$, roughly the gas-phase carbon abundance. The chemistry of dense PDRs is driven by photo-reactions (Sternberg & Dalgarno 1995) and is also characterized by the warm temperatures attained by the gas ($T \simeq 100$–1000 K) and by a large fraction of (FUV-pumped) vibrationally excited molecular hydrogen, H_2^* (e.g., Black & van Dishoeck 1987).

Despite the large FUV radiation fields, H_2 molecules form on the surfaces of relatively warm dust grains ($T_{dust} \gtrsim 50$ K for $\chi \gtrsim 10^3$; e.g., Cazaux & Tielens 2004, Bron et al. 2014 and references therein). As the H_2 abundance increases from the PDR edge to the cloud interior, reactions of H_2 with neutral and singly ionized atoms initiate the chemistry and lead to the formation of hydrides. Owing to the higher gas and electron densities compared with diffuse clouds, the excitation temperatures rise above the background temperature and rotational line emission is observed. Recent detections in dense PDRs include NH_3, CH^+, SH^+, OH^+, H_2O, OH, HF, CH and H_2Cl^+ (e.g., Batrla & Wilson 2003; Habart et al. 2010; Goicoechea et al. 2011; Nagy et al. 2013; van der Tak et al. 2012, 2013; Neufeld et al. 2012).

4.1. The Role of Vibrationally Excited H_2 in Chemistry

The absorption of FUV photons in the Lyman ($B\,^1\Sigma_u - X\,^1\Sigma_g^+$) and Werner ($C\,^1\Pi_u - X\,^1\Sigma_g^+$) bands produces molecular hydrogen in excited electronic states. 10% of absorptions are followed by emission into the unbound continuum, leading to the dissociation of the molecule. 90% of absorptions, however, are followed by rapid radiative decay to the ground electronic state X (see an early historical review by Field et al. 1966 and later quantitative developments by, e.g., Black & Dalgarno 1976 and references therein.) PDRs thus naturally produce large fractional abundances, $f^* = n(H_2\ v \geq 1)/n(H_2\ v = 0)$, of vibrationally excited molecular hydrogen, H_2^*. In low-density PDRs ($\lesssim 10^4$ cm^{-3}), H_2 is excited by FUV absorption followed by radiative fluorescent emission. The main gas-heating mechanism is the photoelectric effect on PAHs and grain surfaces. For higher gas densities, collisional deexcitation through inelastic H-H_2 and H_2-H_2 collisions start to be important, and collisional deexcitation of FUV-pumped H_2 can dominate the gas heating. In addition, pure rotational lines of HD (Wright et al. 1999) and H_2 (Allers et al. 2005) can be detected. Their low critical densities make them good diagnostics of the warm gas temperature.

The H_2 $v = 1$ levels have energies greater than 0.5 eV (~5800 K) above the ground state $v = 0$, and this energy can be used to overcome the endothermicity (or energy barrier) of chemical reactions involved in the formation of some hydrides, thus enhancing their production rate in PDRs. A very favorable case is CH^+. As previously noted, the $C^+ + H_2 \rightarrow CH^+ + H$ reaction is endothermic by ~4300 K (see **Figure 2**); temperatures greater than 1,000 K are required to produce significant amounts of CH^+ when H_2 is in the $v = 0$ state. Laboratory experiments (Hierl et al. 1997) and quantum calculations (e.g., Zanchet et al. 2013b), however, show that the reaction becomes exothermic when H_2^*, rather than $H_2(v = 0)$, is the reactant. The reaction rate k^* then reaches the Langevin limiting case and becomes almost independent of the temperature. In practice, enhanced XH^+ (or XH) hydride abundances will be produced through reactions

Atacama Large Millimeter/submillimeter Array (ALMA): an ensemble of 66 (sub)millimeter telescopes operating between 80 and 900 GHz

$X^+ + H_2^* \rightarrow XH^+ + H$ (or $X + H_2^* \rightarrow XH + H$) if the product $f^* \Delta k(T)$ is larger than 1. Here, $\Delta k(T) = k^*(T)/k^0(T)$ is the reaction rate ratio when H_2 is in a vibrationally excited state and the reactants are in the ground state (see Agúndez et al. 2010). In addition, $k^*(T)$ (the specific reaction rate with H_2^*) has to be large enough compared to other reactions removing the atom X^+ (or X)—for example, X^+ neutralization reactions with PAHs and small grains.

Rotationally excited CH^+ emission lines were first detected toward planetary nebula NGC 7027 (Cernicharo et al. 1997). These lines arise from the warm and dense PDR surrounding the ionized nebula that is irradiated by the strong UV field from the hot central star ($T_{\rm eff} \approx$ 200,000 K). The same pure rotation emission lines have been detected in the Orion Bar (Nagy et al. 2013, shown in **Figure 8**, right panel) and in the irradiated surface of the protoplanetary disk around Herbig Be star HD 100546 (Thi et al. 2011). As there is no reaction pathway that can efficiently produce CH^+ in FUV-shielded cold gas, CH^+ is expected to peak near the PDR edge where C^+ and H_2^* are abundant (see **Figure 8**, left panel). A similar argument applies to SH^+, with the difference that the $S^+ + H_2 \rightarrow SH^+ + H$ reaction is even more endothermic (~10,000 K) and only becomes exothermic when H_2^* is in the $v = 2$ or higher vibrational states (Zanchet et al. 2013a). Line emission from both ions has been observed in the Orion Bar with *Herschel* (Nagy et al. 2013), and $^{13}CH^+$ and SH^+ can be detected from ground-based telescopes such as ALMA (the Atacama Large Millimeter/submillimeter Array). Rotationally excited CH^+ has also been recently observed in visible absorption (Oka et al. 2013) toward lower-density PDR environments close to hot massive stars, where vibrationally excited H_2 is also observed in FUV absorption (Rachford et al. 2014).

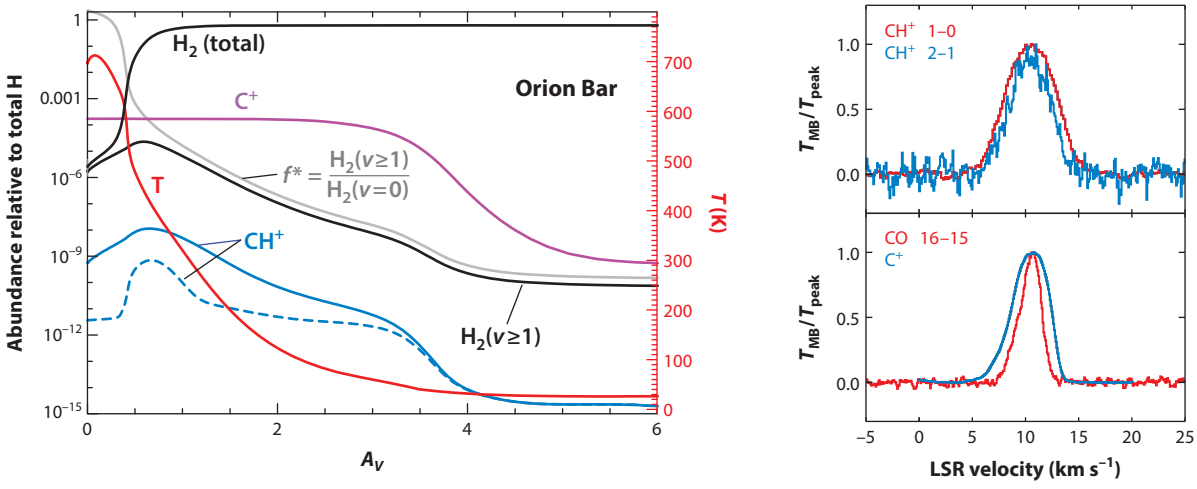

Figure 8

(*Left*) Photodissociation region model adapted to the physical conditions in the Orion Bar: $n_{\rm H} = 10^5$ cm^{-3} and $\chi = 3 \times 10^4$. Abundances relative to $n_{\rm H}$ are shown for H_2, H_2 ($v \geq 1$) = H_2^*, C^+, and CH^+ as a function of depth A_V into the cloud. Also shown is $f^* = n(H_2\ v \geq 1)/n(H_2\ v = 0)$, the fraction of vibrationally excited H_2 with respect to the ground vibrational state, and the gas temperature T. For the CH^+ abundance profile, the dashed line is for a specific model that only considers reactions of C^+ with H_2 in the ground vibrational state ($v = 0$). The continuous curve shows the CH^+ abundance including also state-to-state reactions of C^+ with H_2^*. Adapted from Agúndez et al. (2010) with permission from the AAS. (*Right*) Velocity-resolved observations of the Orion Bar with *Herschel*-HIFI (Heterodyne Instrument for the Far-Infrared). CH^+ J = 1-0 and 2-1 lines are broader than those of [CII] and CO J = 16–15. This may be the signature of formation pumping, as explained at the end of Section 4.3. Abbreviations: LSR, local standard of rest; $T_{\rm MB}$, main beam temperature. Adapted from Nagy et al. (2013) with permission from *Astronomy & Astrophysics*, © ESO.

The role of FUV-pumped H_2^* in PDR chemistry may also be important at the scales of entire molecular cloud complexes. In template star-forming regions such as Orion, over 98% of the large-scale NIR H_2 emission is thought to arise from FUV-excited fluorescent emission in PDR gas (Luhman et al. 1994). This widespread H_2^* emission traces the extended molecular gas that is illuminated by the strong FUV radiation field from massive stars in the Trapezium cluster. Its presence likely explains the large-scale CH^+ $J = 1-0$ emission detected in Orion molecular cloud (J.R. Goicoechea, private communication). The high abundances of H_2^* in local massive star-forming regions may have consequences for the interpretation of hydride spectra in the extragalactic context, as many actively star-forming galaxies are dominated by PDR emission. In diffuse molecular gas (which is much less dense and has lower FUV fluxes), the H_2^* abundance and f^* fractions are significantly lower. Indeed, the large CH^+ and SH^+ column densities inferred from line absorption observations of diffuse clouds cannot be explained by standard PDR models adapted to the $n_H \simeq 100$ cm^{-3} and $\chi \simeq 1$ conditions prevailing in these clouds (e.g., Godard et al. 2012 and references to older models therein).

4.2. Oxygen Hydrides

Relatively low water vapor abundances are expected in dense PDRs. H_2O has a high adsorption energy and freezes at $T_{dust} < 100$ K in dense cloud conditions (as compared to ~20 K for CO). Photodesorption of water ice mantles takes place in PDRs, but H_2O molecules are readily photodissociated by the intense FUV radiation field (Hollenbach et al. 2009). This process results predominantly in OH + H (e.g., van Dishoeck et al. 2013). Low excitation H_2O rotational lines have been observed toward high FUV flux PDRs such as the Orion Bar (Habart et al. 2010, Choi et al. 2014) and Mon R2 (Pilleri et al. 2012). The inferred gas-phase H_2O abundances are less than a few $\times 10^{-7}$. Rotationally excited OH emission lines have been also detected in the Orion Bar. They are consistent with a $OH/H_2O > 1$ column density ratio (Goicoechea et al. 2011), similar to the diffuse cloud values, whereas $OH/H_2O < 1$ ratios are typically observed toward warm shocked gas (see Section 5). Regarding OH formation, the dominant route near the edge of a strongly UV-irradiated PDR is the endothermic reaction $O + H_2 \rightarrow OH + H$ (see the first OH abundance peak in **Figure 5**, right panel). However, the reaction remains slow when the H_2 is vibrationally excited (Sultanov & Balakrishnan 2005). Consequently, the OH formation rate is likely more sensitive to the gas temperature than to the H_2^* abundance. For lower FUV fields and temperatures, OH forms from H_3O^+ electron recombination and from grain surface reactions (e.g., Hollenbach et al. 2009, 2012).

In the Milky Way, OH^+ rotational line emission has been detected toward high electron density environments: the Orion Bar (van der Tak et al. 2013), planetary nebulae hosting hot central stars with $T_{eff} > 100{,}000$ K (Aleman et al. 2014), and the supernova remnant in the Crab Nebula (Barlow et al. 2013). The nondetection of H_2O^+ and H_3O^+ emission in these environments indicates that OH^+ lines arise in gas layers where most hydrogen is in atomic form and OH^+ is predominantly formed by the $O^+ + H_2 \rightarrow OH^+ + H$ exothermic reaction. **Figure 5** (left panel) shows predictions of a steady-state PDR model for an $n_H = 10^4$ cm^{-3} cloud illuminated by an FUV field that is 100 times the mean interstellar radiation field. These conditions are representative of a molecular cloud close to massive O and B stars. The model includes reactions with PAHs and freeze-out of gas-phase species (important at $A_V > 4$). It shows that OH^+ peaks closer to the PDR edge than other oxygen hydrides. **Figure 5** (right panel) shows the results for a higher density, $n_H = 10^6$ cm^{-3}, and higher FUV irradiation model, $\chi = 10^5$. These conditions are more typical of the compressed PDR layers at the boundary of an HII region surrounding a massive star or the surface layers of protoplanetary disks. In this model, H_2 collisional deexcitation dominates the gas

heating, and the gas attains high temperatures ($T \simeq 1000$ K at $A_V \simeq 1$). This triggers a warm gas phase in which many endothermic reactions can proceed rapidly. The dense PDRs located at the walls of outflow cavities irradiated by a high-mass young stellar object have been modeled by Bruderer et al. (2010), who predicted high abundances of CH^+, OH^+ and NH^+ within such regions.

4.3. Formation Pumping and the Excitation of Reactive Hydride Ions

Reactive collisions (collisions that lead to a chemical reaction) influence the excitation of molecules when the timescale of the chemical reaction becomes comparable to, or shorter than, that of nonreactive collisions. This makes the lifetime of the molecule so short that it does not get thermalized by collisions with nonreactive species or by radiative absorptions of the background radiation field. This is referred to as formation pumping: The molecule retains an excited state after its formation, and a proper treatment of the molecule excitation requires including chemical formation and destruction rates in the statistical equilibrium calculation that determines the level populations (e.g., Black 1998). Reactive ions such as CH^+ or OH^+ are special because they can be destroyed on nearly every collision with the most abundant species: H_2, H, and e^- (however, OH^+ does not react with H). Detailed CH^+ excitation models show that formation pumping is the main contributor to the population of CH^+ rotationally excited levels in PDRs such as the Orion Bar (Godard & Cernicharo 2013). In addition, the effects of molecule destruction and molecule formation in excited levels need to be taken into account in chemical networks. It is becoming common to refer to state-to-state chemistry when the specific state-dependent reaction rates are included in models.

Reactions of C^+ with $H_2(v = 0, J > 7)$ or with $H_2(v \geq 1)$ are exothermic and drive the CH^+ production in PDRs such as the Orion Bar (see Section 4.1). Therefore, CH^+ formation results in an energy excess equivalent to several thousand K. This energy may be redistributed into translational motion of the newly formed CH^+ molecules (Black 1998). CH^+ reacts so quickly with H, H_2, and electrons that its translational motions may never thermalize to the gas kinetic temperature. The broader CH^+ $J = 1–0$ emission line widths observed toward the Orion Bar ($\sim$5.5 km s^{-1}, corresponding to a temperature of several thousand K) compared with those of other molecular lines (usually $\sim$2–3 km s^{-1}; see **Figure 8**, right panel) have been interpreted as the signature of CH^+ formation pumping and of nonthermal velocity distributions (Nagy et al. 2013). Formation pumping also influences OH^+ excitation (Gómez-Carrasco et al. 2014) and may also explain the broad OH^+ emission lines (van der Tak et al. 2013).

5. HYDRIDES IN SHOCKS AND TURBULENT DISSIPATION REGIONS

5.1. Shocks

Several astrophysical phenomena—including protostellar outflows and supernovae—give rise to supersonic motions in the ISM, and these motions can drive shock waves that heat and compress the gas. Such shock waves modify the chemistry of and the emission from interstellar hydrides, greatly enhancing the abundances of certain species, populating high-lying rotational states, and triggering strong maser amplification in specific transitions of OH and H_2O.

The chemical effects of shock waves include the sputtering of dust grains, which releases grain materials into the gas phase, and the enhancement of gas-phase endothermic reactions that are negligibly slow at the typical temperatures ($T \leq 80$ K) of cold interstellar gas clouds but can become rapid behind shock waves. In dense molecular clouds, where dust grains are coated with icy

grain mantles, the sputtering of grain mantles has a profound effect on the water vapor abundances behind shocks. The sputtering process has been the subject of several theoretical studies (Draine et al. 1983, Jiménez-Serra et al. 2008, Gusdorf et al. 2008) that suggest that grain mantles are completely removed in shocks propagating at velocities larger than ∼20–25 km s^{-1}, resulting in the release of water and other volatile grain mantle materials into the gas phase. Observationally, the interstellar water vapor abundance measured by satellite observatories such as the *Submillimeter Wave Astronomy Satellite*, *Odin*, and *Herschel* is known to vary by more than three orders of magnitude (see van Dishoeck et al. 2013 and references therein), with the largest abundances observed in warm shocked regions associated with protostellar outflows and supernova remnants. In these regions, the water vapor abundance can reach several $\times 10^{-4}$ relative to hydrogen nuclei, an abundance comparable to that of carbon monoxide. However, many measurements of the water vapor abundances in shocked regions (see table 4 in van Dishoeck et al. 2013) are considerably smaller and lie below the predictions for shocks capable of sputtering icy grain mantles. This discrepancy may reflect the fact that many abundance determinations are averages over a mixture of shocks of varying velocity, some of which are too slow to sputter mantles, or the discrepancy may be due to UV irradiation of the shocked gas lowering the H_2O abundance and enhancing OH (Karska et al. 2014, Goicoechea et al. 2015). In a recent study (Neufeld et al. 2014) of the FIR line emission detected by *Herschel* and *Spitzer* from shocked gas in NGC 2071, W28, and 3C391, the relative line intensities for multiple transitions of H_2O, CO, and H_2 were found to be in acceptable agreement with standard theoretical models for nondissociative shocks that predict the complete vaporization of grain mantles in shocks of velocity ∼25 km s^{-1}, behind which the characteristic gas temperature is ∼1300 K and the H_2O/CO ratio is 1.2.

The second chemical effect of shock waves is to selectively increase the abundances of molecules that can be produced rapidly by endothermic reactions that are slow at the temperatures of cold quiescent gas clouds. Behind shock waves, elevated gas temperatures of a few $\times 10^2$–10^3 K can be sufficient to overcome the barriers for several of the endothermic H-atom abstraction reactions listed in **Figure 2**, greatly increasing the predicted abundances of CH^+, SH^+, CH, SH, OH and H_2O. In addition to the effects of the elevated temperatures behind interstellar shock waves, velocity drifts between the ions (which are coupled to the magnetic field) and the neutral species (which are not) can lead to an additional enhancement in the rates of ion-neutral reactions. MHD shock waves propagating at ∼10 km s^{-1}, in which such velocity drifts are present, have been invoked (e.g., Draine & Katz 1986; Pineau des Forêts et al. 1986a,b) to explain large discrepancies between the observed abundances of CH^+, SH^+, and SH in diffuse molecular clouds and the predictions of standard photochemical models for cold ($T \leq 80$ K) diffuse gas.

In addition to their chemical effects, shock waves propagating in dense molecular gas also populate high-lying rotational states of hydrides that lead to a distinctive emission spectrum dominated by high-lying, collisionally pumped rotational transitions of H_2, CO, H_2O, and OH (Chernoff et al. 1982, Draine & McKee 1993). **Figure 9** shows a comparison of the FIR spectra of three environments: a molecular outflow and associated shocked gas, a sight line to the Galactic Center including dense gas and foreground absorption by diffuse gas, and a highly UV-irradiated, dense PDR. Whereas the shocked region shows intense OH and H_2O emission lines, the dense and warm environment of the Galactic Center region has a more diverse spectrum with other hydrides such as NH_3, H_3O^+, and H_2O^+, indicating the presence of UV- and CR-irradiated molecular gas. The PDR spectrum is dominated by strong [CII] and [OI] emission, with faint lines from H_2O and rotationally excited CH^+.

In the case of OH, mid-IR transitions with upper-state energies (E_u/k_B) of several $\times 10^4$ K can also be excited following the photodissociation of H_2O by shock-generated UV radiation; this phenomenon, observed by *Spitzer* toward HH 211 and illustrated in **Figure 10** (Tappe et al.

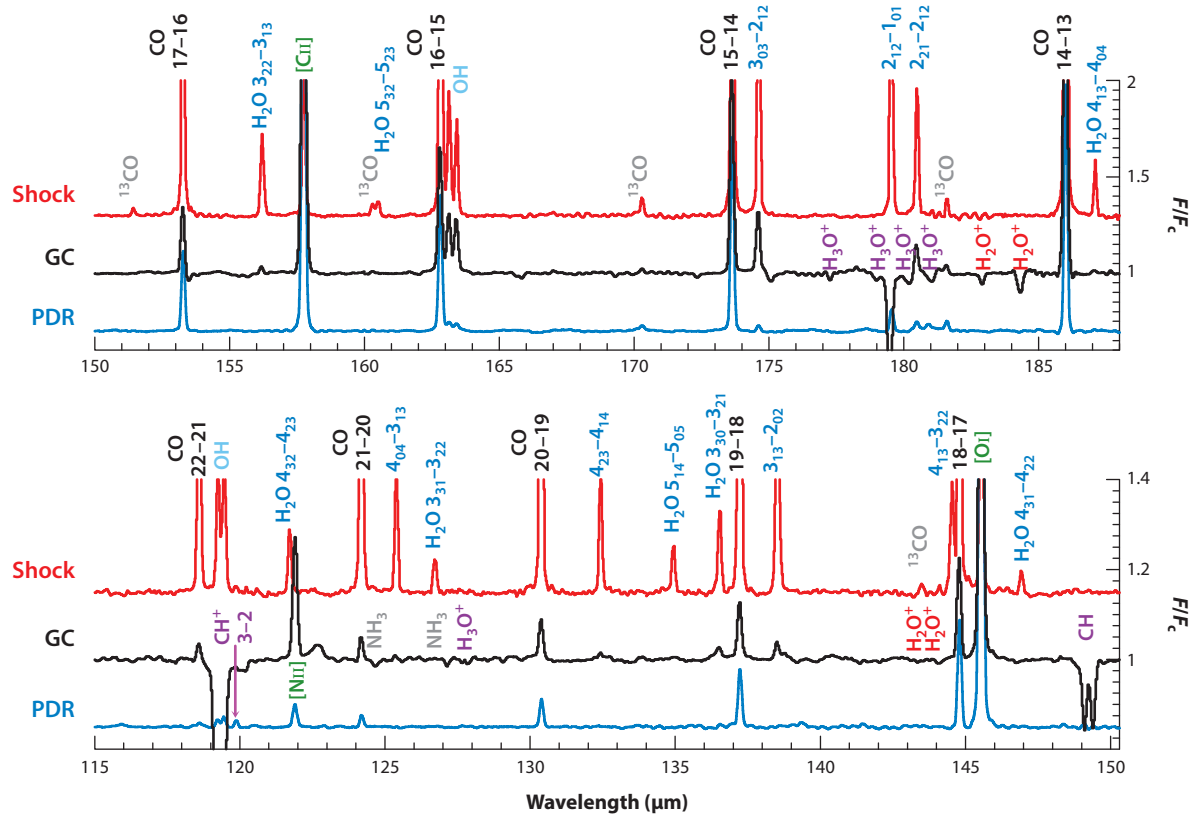

Figure 9

Comparative FIR spectra of three template environments in the Milky Way taken with *Herschel*'s Photoconductor Array Camera and Spectrometer between 115 μm and 188 μm: a molecular outflow and associated shocked gas, the Galactic Center (GC), and a highly UV-irradiated photodissociation region (PDR). They correspond, from top to bottom, to Orion Becklin-Neugebauer/Kleinmann-Low outflows (*red*, Goicoechea et al. 2015), the circumnuclear disk around Sgr A* (*black*, Goicoechea et al. 2013), and the Orion Bar PDR (*blue*, C. Joblin, manuscript in preparation). The *y*-axis shows the line flux to continuum flux ratio, and the *x*-axis is the wavelength in microns. The shock and PDR spectra have been shifted from the $F/F_c = 1$ level for clarity.

2008), occurs because the photodissociation of H_2O following absorption of Lyman alpha radiation leaves OH in states of rotational quantum number 30–50. Along with the normal (noninverted) OH and H_2O line radiation emitted by warm shocked regions, strong maser action is observed in several transitions: These include the 22-GHz $6_{16}–5_{23}$ transition of H_2O, frequently observed from outflow-driven shock waves along with several submillimeter water maser transitions (e.g., Neufeld et al. 2013 and references therein), and the 1,720-MHz transition of OH, a signpost of supernova-driven shock waves (e.g., Frail & Mitchell 1998). Maser lines are typically characterized by small spots of emission that are often unresolved even in long-baseline interferometric observations, narrow line widths, and variability on timescales of months or less. Emission in the 22-GHz water maser transition, in particular, can achieve extraordinarily high brightness temperatures that may exceed 10^{14} K. Theoretical models for water maser emissions invoke either fast, dissociative jump (J-type) shocks (Elitzur et al. 1989, Hollenbach et al. 2013), or slower, nondissociative C-type shocks in which the fluid velocities vary continuously (Kaufman & Neufeld 1996). Where multiple water maser transitions are observed, maser line ratios can provide constraints on

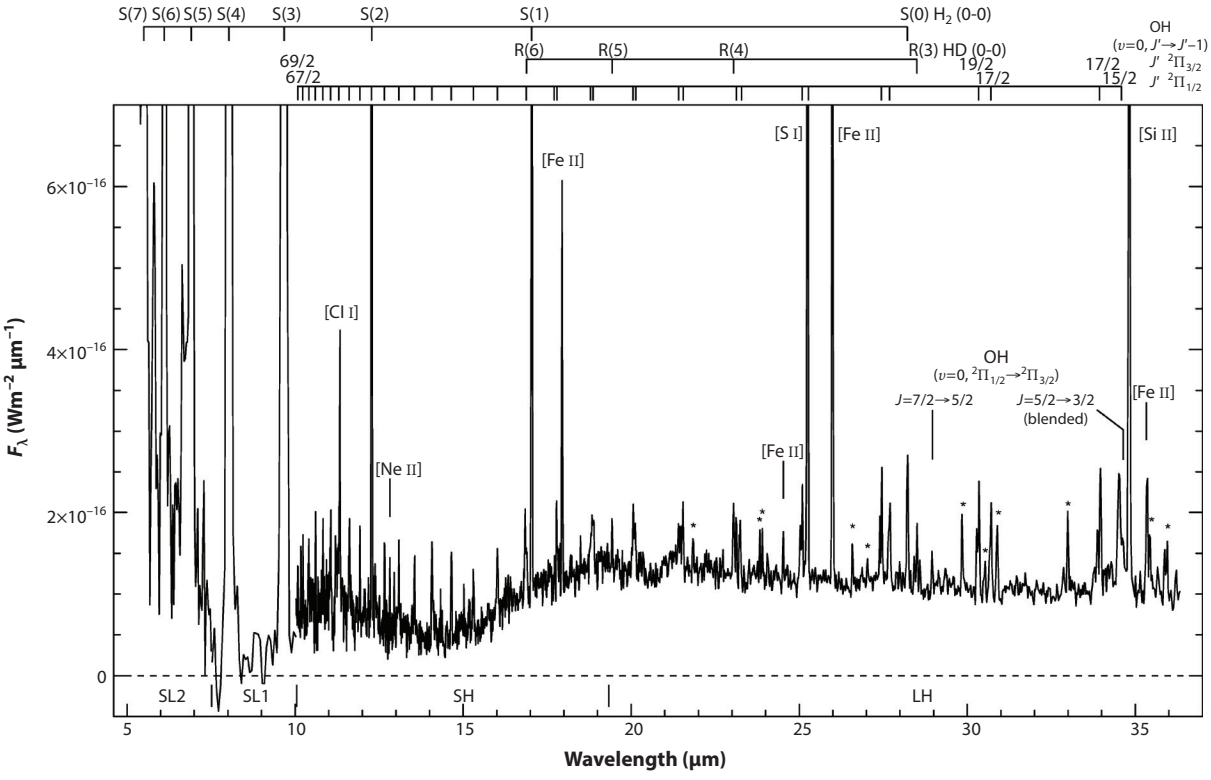

Figure 10

Spitzer spectrum obtained toward HH 211. Pure rotational lines of OH, with upper states with J up to 69/2, are clearly detected. Features marked with an asterisk are pure rotational transitions of H_2O. SL2, SL1, SH, and LH are modules of the *Spitzer* IRS (Infrared Spectrograph). Adapted from Tappe et al. (2008) with permission from the AAS.

the gas temperature in the masing region and the nature of the shocks that are present. Paradoxically, nondissociative shocks can produce hotter molecular material than faster dissociative shocks, where molecules are quickly destroyed behind the shock front and are reformed only after the gas has cooled to ∼500 K. In some maser sources, gas temperatures of at least 900 K are implied by the observed water maser line ratios, indicating the presence of nondissociative shocks (Melnick et al. 1993). Where supernova-driven shock waves encounter molecular clouds, widespread 1720 MHz OH maser emission is observed; in this environment, the enhanced column densities of OH needed to explain the observed maser emission are believed to result from the effects of X-rays and/or CRs in dissociating H_2O to form OH (Wardle & Yusef-Zadeh 2002).

5.2. Turbulent Dissipation Regions

Turbulent dissipation regions (TDRs; Godard et al. 2009, 2012, 2014) represent an alternative but related scenario in which endothermic reaction rates can be enhanced as a result of locally elevated gas temperatures and ion-neutral drift. In this scenario, molecules are produced in TDRs, represented as vortices in which the ion-neutral drift is induced by the ambient magnetic field. Model parameters include the physical conditions in the ambient medium (represented by parameters n, χ, A_V, and ζ) along with four adjustable variables describing the turbulence dissipation rate, the

TDR: turbulent dissipation region

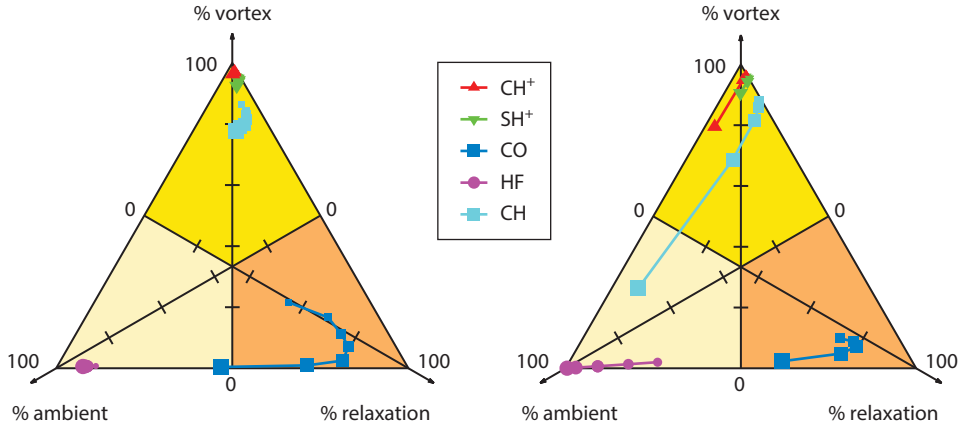

Figure 11

Ternary diagrams for the turbulent dissipation region model of Godard et al. (2014), indicating the fraction of each of five diatomic molecules (CH^+, SH^+, CO, HF, and CH) found in three components of a diffuse cloud, (*a*) ambient material currently unaffected by turbulent dissipation (*pale yellow*), (*b*) material within the vortices that are the assumed sites of turbulent dissipation in this model (*bright yellow*), and (*c*) material that has passed through a dissipative vortex and is currently relaxing to the ambient chemistry (*orange*). The left panel displays model results for a gas density of $n_H = 50\,cm^{-3}$, and for several values of the visual extinction, A_V : In order of increasing symbol size, 0.1, 0.2, 0.3, 0.4, 0.6, 0.8, and 1.0 mag are shown. The right panel displays results for several values of the density, n_H: 20, 30, 50, 100, and 300 cm^{-3}, at $A_V = 0.4$ mag. Adapted from Godard et al. (2014) with permission from *Astronomy & Astrophysics*, © ESO.

ion-neutral drift, the vortex magnitude, and the vortex lifetime. Given reasonable assumptions about the parameters that describe the turbulence, TDR models have been successful in accounting for the observed abundances of CH^+, SH^+ and SH in diffuse molecular clouds. **Figure 11** consists of two ternary diagrams (adapted from Godard et al. 2014) showing, for five diatomic molecules, the relative fractions of the total column density in three separate components: (*a*) ambient material currently unaffected by turbulent dissipation, (*b*) material within the vortices that are the assumed sites of turbulent dissipation in this model, and (*c*) material that has passed through a dissipative vortex and is currently relaxing to the ambient chemistry (relaxation). This model indicates that the CH^+ and SH^+ column densities are dominated by material in dissipative vortices (component *b*); the HF column density, by contrast, originates primarily in the ambient gas (component *a*). The behavior of CH depends on the density, with the dominant component switching from the vortices (component *b*) to the ambient gas (component *a*).The different behaviors predicted for the four hydrides reflect the fact that the production of CH, CH^+ and SH^+ is endothermic, whereas that of HF is exothermic. Whereas the extensive chemical calculations leading to the results shown in **Figure 11** are based on a simple characterization of interstellar turbulence with several adjustable parameters, a complementary approach makes use of more sophisticated numerical simulations of turbulence (Myers et al. 2015). To date, studies adopting the latter approach have included a more limited chemistry focused on the CH^+ problem.

In both shocks and TDRs, the dynamical timescales can be short compared with the time needed to establish a chemical equilibrium in which the rates of molecular formation and destruction are equal; a time-dependent treatment of the chemical rate equations is therefore needed. Simple shock models are sometimes described as steady-state models if the physical and chemical conditions are nonvarying in a particular inertial frame, but this is distinct from a chemical quasi-equilibrium in which the net rates of formation and destruction are nearly equal for each species. We note

also that in this context, a chemical quasi-equilibrium, which is often a good approximation where shocks and TDRs are absent, is quite different from TE, in which the rate of every chemical process equals that of its reverse process and the molecular abundances are determined solely by thermodynamics. The condition of TE never applies in the ISM because of the presence of CRs and, in diffuse and translucent interstellar clouds, of UV radiation that would be entirely absent in thermal equilibrium at the gas kinetic temperature.

6. HYDRIDES IN DENSE AND SHIELDED GAS

Many neutral hydrides stay abundant in shielded regions, even in dense prestellar and protostellar cores. At the low gas and dust temperatures of these regions (~10 K), molecules freeze on dust grains, building an ice layer. Ice mantles also grow thanks to the condensation of atoms, which contribute to the formation of saturated hydrides by hydrogenation: H_2O for oxygen, CH_4 for carbon and NH_3 for nitrogen. **Figure 12** shows a representative IR spectrum of a massive star-forming region with prominent absorption features tracing the composition of the ice mantle. Water ice is the dominant species, with NH_3 and CH_4 abundances only a few percent of the water ice (Boogert et al. 2015).

The low temperatures ($T \sim 10$ K) and absence of FUV radiation represent a favorable environment for fractionation, the chemical process leading to a higher fraction of an isotope in a given molecule (an isotopologue) than the ratio of the elemental abundances. The most efficient process is deuterium fractionation, in which one or several hydrogen atoms are substituted by

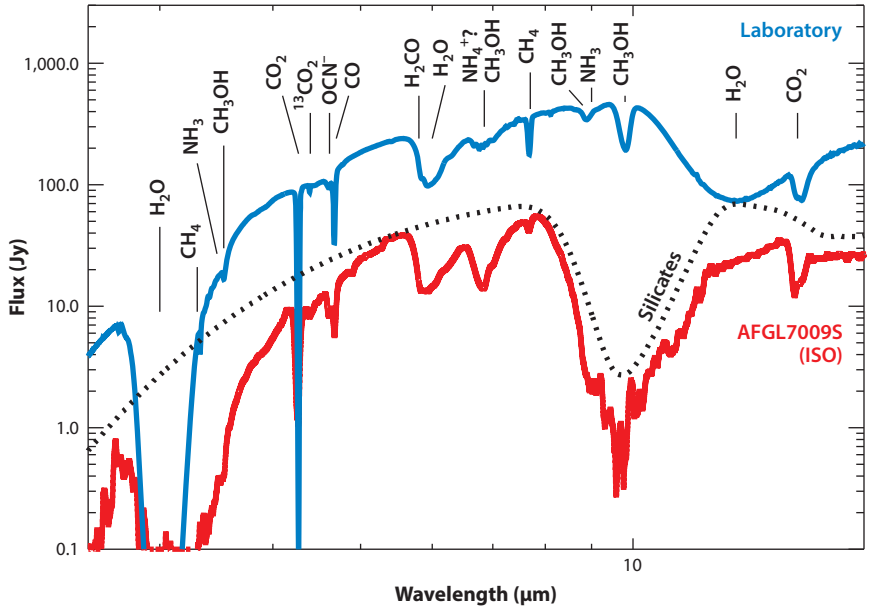

Figure 12

Comparison between the ISO-SWS (*Infrared Space Observatory*-Short Wavelength Spectrometer) spectrum toward the massive protostar AFGL7009S (*red line*) and a laboratory transmission spectrum (*blue line*). The dotted line shows the dust continuum, including absorption from silicates. The positions of the main ice constituent absorption lines are indicated, including the tentative identification of solid NH^{4+} in the ice mantle. Adapted from Dartois et al. (1998) with permission from *Astronomy & Astrophysics*, © ESO.

deuterium atoms. As reviewed by Caselli & Ceccarelli (2012), deuterium fractionation can be very efficient in cold regions, with several molecules reaching abundance ratios [XH]/[XD] exceeding one percent, while the elemental D/H ratio is approximately 2×10^{-5}. Fractionation may also involve other isotopes such as ^{13}C, ^{18}O, ^{17}O or ^{15}N. Fractionation in D and ^{15}N is studied to relate ISM processes with the formation of the first solids in the solar system because primitive material shows localized D and ^{15}N enhancements (Aléon 2010).

In the dense gas around protostars [$n(H_2) > 10^7$ cm^{-3}], the dust temperature increases up to the ice sublimation threshold ($T \sim 100$ K for water ice). The gas-phase abundances of neutral hydrides significantly increase in these hot cores (for massive stars) and hot corinos (for low-mass stars). These objects exhibit a rich spectrum, including numerous hydride emission lines at (sub)millimeter wavelengths (e.g., **Figure 9**) and absorption lines in the IR, revealing a high abundance of water vapor (Boonman et al. 2003), methane, and CH_3 (e.g., Knez et al. 2009) in the hot gas within a few hundred AU of the protostar. Highly excited NH_3 inversion lines at centimeter wavelengths also trace the same region (Goddi et al. 2015). Such spectra provide key information about the temperature and velocity field in the vicinity of the protostars.

Hydrides, especially water and OH, are interesting probes of protoplanetary disks because different lines can be used to probe different regions: ground state lines trace the cold outer regions of the disk, whereas excited lines trace the illuminated surface closer to the central protostar. Following the first detections of water vapor in the inner region (within a few AU) (e.g., Salyk et al. 2008, Carr & Najita 2008), *Herschel*-PACS (Photoconductor Array Camera and Spectrometer) spectroscopy in the FIR has confirmed the presence of OH and H_2O in protoplanetary disks around both T Tauri and Herbig AeBe stars, the latter having a higher OH/H_2O abundance ratio than the former (Fedele et al. 2013). Both *ortho*- and *para*-H_2O ground-state lines have been detected by *Herschel*-HIFI toward TW-Hya (Hogerheijde et al. 2011). Most of the water is frozen as ice in the disk midplane, and water vapor represents a very minor fraction of the water reservoir. Because of the high line opacity, the interpretation of the detected signals requires a good understanding of the disk geometry and sophisticated radiative transfer calculations. Other *Herschel* detections include CH^+ tracing the UV-irradiated disk surface, and *o*-NH_3 associated with cool layers (Thi et al. 2011).

6.1. Water and Oxygen Hydrides

In dense gas, water is the main oxygen hydride, together with hydroxyl radical OH and their deuterated counterparts HDO, D_2O, OD, while the main ion is H_3O^+. Although water ice is ubiquitous in molecular clouds, with a detection threshold of approximately three magnitudes of visual extinction (Whittet et al. 2013), the detection of water vapor in cold cores is very challenging because of the need for a space-based observatory combining high sensitivity and high spectral resolution. Thanks to *Herschel*-HIFI, water vapor was detected toward the L1544 prestellar core (Caselli et al. 2012). The line profile shows an inverse P-Cygni profile, with a blueshifted emission peak and redshifted absorption tracing the slow gravitational collapse of this core. Although the water abundance relative to H_2 is very small, approximately 10^{-9}, the mere presence of water vapor in such a cold ($T = 7$ K) and dense [$n(H_2) > 10^6$ cm^{-3}] environment indicates that the desorption induced by the secondary FUV photons ($\chi = 10^{-4}$, Prasad & Tarafdar 1983) produced during the interaction of CRs with molecular hydrogen is efficient. This observation is consistent with predictions from chemical models such as those shown in **Figure 5**, where water vapor is present at a cloud depth of a few magnitudes of extinction (Hollenbach et al. 2012). In dense, cold gas, water is cycled between the gas and solid phase through H_3O^+. Hence, the water OPR is expected to deviate from thermal equilibrium in a similar way as the OPR for NH_3 (Sipilä et al.

2015). Observations of H_3O^+ or of its deuterated counterparts H_2DO^+, HD_2O^+, and D_3O^+ could provide further constraints on the CR ionization rate. Although no detection toward cold cores has been achieved so far, several H_3O^+ lines show up in emission toward massive star-forming regions tracing the presence of energetic radiation and/or CRs produced by the embedded protostar (Benz et al. 2013).

Although most rotational water lines are not observable from the ground because of the presence of water vapor in the Earth atmosphere, atmospheric transmission is good for rotational lines of heavy water. Both HDO (Beckman et al. 1982) and D_2O (Butner et al. 2007) are present with a moderate level of fractionation. The number of measurements of HDO/H_2O and D_2O/HDO abundance ratios in the same source is small. In Orion-KL, the prototypical hot core, HDO/H_2O $\sim 3 \times 10^{-3}$, a factor of 2 larger than D_2O/HDO (Neill et al. 2013). Most species show a D/H ratio in the range 2–8 $\times 10^{-3}$ in this source. As reviewed by Caselli & Ceccarelli (2012), the deuterium fractionation of water vapor is a complex phenomenon, because it is controlled by both solid-phase and gas-phase processes and is likely time-dependent, given the similarity of the chemical timescales to the free-fall time of dense cores. The OD radical has been detected with the SOFIA airborne observatory in the cold envelope surrounding the low-mass protostar IRAS16293-2422 (Parise et al. 2012). The large OD/HDO abundance ratio (OD/HDO = 20–90) remains to be fully explained. The dissociative recombination of H_2DO^+ may contribute to the OD enhancement, but a quantitative assessment awaits a measurement of the branching ratios toward HDO and OD. Because of their large critical densities and upper energy levels, the only HDO transitions detectable in cold cores are the two ground-state transitions at 465 GHz ($1_{01}-0_{00}$) and 894 GHz ($1_{11}-0_{00}$). In hot cores and hot corinos, the conditions are favorable for collisional excitation of many HDO levels, leading to a richer spectrum. For a collapsing core around a massive protostar, the HDO ground-state transitions are particularly sensitive to the velocity field in the collapsing envelope, whereas the excited lines probe the hot inner region (e.g., Coutens et al. 2014). Like H_2O, D_2O has two spin symmetry states, with *p*-D_2O the more stable species. *o*-D_2O has its lowest rotational state at an energy 17 K above that of *p*-D_2O, and *ortho* states have a spin degeneracy twice that of *para* states. From *Herschel* observations of both *p*-D_2O and *o*-D_2O, Vastel et al. (2010) concluded that the OPR is consistent with the statistical value of two.

6.2. Methane and Carbon Hydrides

As it is for oxygen hydrides, the competition between condensation and desorption is also important for carbon hydrides in dense and FUV-shielded gas. There are, however, two important differences with oxygen: (*a*) The carbon reservoir is CO and not methane, and (*b*) carbon hydride radicals (CH, CH_2, and CH_3) and ions (CH_3^+) initiate the organic chemistry and therefore play a pivotal role in the formation of a large fraction of the molecules present in the ISM. Another interesting property of the methylidyne radical, CH, is the linear scaling of its column density (deduced from the intensity of its Λ-doubling transitions at 3.3 GHz) with that of H_2 up to $A_V \sim 3$ mag (Mattila 1986, Chastain et al. 2010). Although these lines are inverted, with negative excitation temperatures, their integrated intensity approximately scales with the CH column density (Liszt & Lucas 2002). *Herschel* observations of the CH ground-state rotational lines confirm this behavior: toward the low-mass protostar IRAS16293-2422, CH probes the cold envelope (Bottinelli et al. 2014), whereas in more massive sources, CH shows a combination of emission and absorption features (Gerin et al. 2010b), indicating that CH is present in the dense material. The methylene radical, CH_2, shares the same chemistry as CH. Its ground-state transition has been detected by the *Infrared Space Observatory* (ISO) (Polehampton et al. 2005) following its identification in Orion-KL (Hollis et al. 1995).

Methane is best probed by IR spectroscopy using either ground- or space-based telescopes observing the 8 μm region (Lacy et al. 1991, Öberg et al. 2008). Frozen methane has an abundance ∼5% that of water ice, supporting the theory of a formation process involving sequential hydrogenation of carbon on grain surfaces. The gas-phase abundance is more uncertain and ranges between 10^{-6} and 10^{-8} relative to H_2. Even at the highest abundances, most of the interstellar methane is in solid form.

Deuterium fractionation is predicted to be very efficient for carbon hydrides because deuterated methylium, CH^2D^+, can easily exchange its deuterium atom with neutral species. CH_2D^+ is operating in lukewarm regions ($T \sim 30$–70 K) where the kinetic temperature is too high for H_2D^+ to be enriched. The DCN and HDCO molecules are typical products of CH_2D^+-induced chemistry, with observed fractionation levels consistent with chemical models (Roueff et al. 2013). Unfortunately, no astronomical detection of the related species CD and CHD has been reported so far. Further tests involve the search for CH_2D^+. Its rotational spectrum has been measured by Amano (2010), and a tentative detection has been reported toward Orion-KL by Roueff et al. (2013), which awaits confirmation from observations of a less spectrally crowded region. Because of its small dipole moment of 0.3 debye, CH_2D^+ rotational lines are weak at the predicted abundance level. Deuterated methane, CH_3D, has a nonzero but small dipole moment (0.0057 debye), allowing observations of rotational transitions from the ground. After a very deep integration, Sakai et al. (2012) report a tentative detection toward the IRAS04368 + 2557 protostar in the L1527 core. Further searches for CH_3D are needed to confirm this detection, which implies rather large CH_3D (∼3×10^{-7}) and CH_4 (∼4×10^{-6}) gas-phase abundances and very little methane left on grain mantles.

6.3. Ammonia and Nitrogen Hydrides

Nitrogen hydrides are mainly formed in the gas phase through a chain of hydrogen abstraction reactions starting from $N^+ + H_2 \rightarrow NH^+ + H$. This reaction is slightly endothermic (**Figure 2**) and therefore is more efficient for *o*-H_2 than for *p*-H_2. Because of the rather low formation rate in *p*-H_2 enriched gas, a formation route on grain surfaces has also been suggested. Subsequent hydrogen abstraction reactions $NH_n^+ + H_2 \rightarrow NH_{n+1}^+ + H$ with $n = 1, 2, 3$, followed by dissociative recombination reactions, lead to the molecular ions NH_2^+, NH_3^+, and NH_4^+ and the neutral hydrides NH, NH_2, and NH_3. The detection of NH_3D^+ by Cernicharo et al. (2013) nicely confirms this theoretical scheme. NH is also formed as a secondary product of the dissociative recombination reaction of N_2H^+ (Vigren et al. 2012). In dense clouds, the abundances of nitrogen hydrides are dominated by ammonia, with $NH{:}NH_2{:}NH_3 = 3{:}1{:}19$ for the dense core around the protostar IRAS16293-2422 (Le Gal et al. 2014). The excess of NH compared with NH_2 is explained by its additional formation route from the dissociative recombination of N_2H^+.

Ammonia has two spin symmetry states: *o*-NH_3, with K values in multiples of three and $K = 0$; and *p*-NH_3, for other K values. The energy difference between *o*-NH_3 and *p*-NH_3 is 21.5 K, and the high-temperature value of the OPR ratio is 1, whereas an excess of *o*-NH_3 is expected at temperatures lower than 50 K. As a symmetric top with two equilibrium configurations, ammonia exhibits inversion transitions between equivalent rotational states. Whereas the low-energy NH_3 inversion transitions probe the *para* species, the first *o*-NH_3 state accessible from the ground is the $(J, K) = (3, 3)$ level at 120 K above the ground level. Therefore, most NH_3 measurements in dense cores only trace *p*-NH_3, and the total ammonia column density is derived assuming an OPR of one. Using *Herschel* absorption data on *o*-NH_3 and *p*-NH_3, Persson et al. (2010) measured an anomalous value of the OPR ratio of 0.7. In *p*-H_2–enriched gas, the chain of ion-molecule

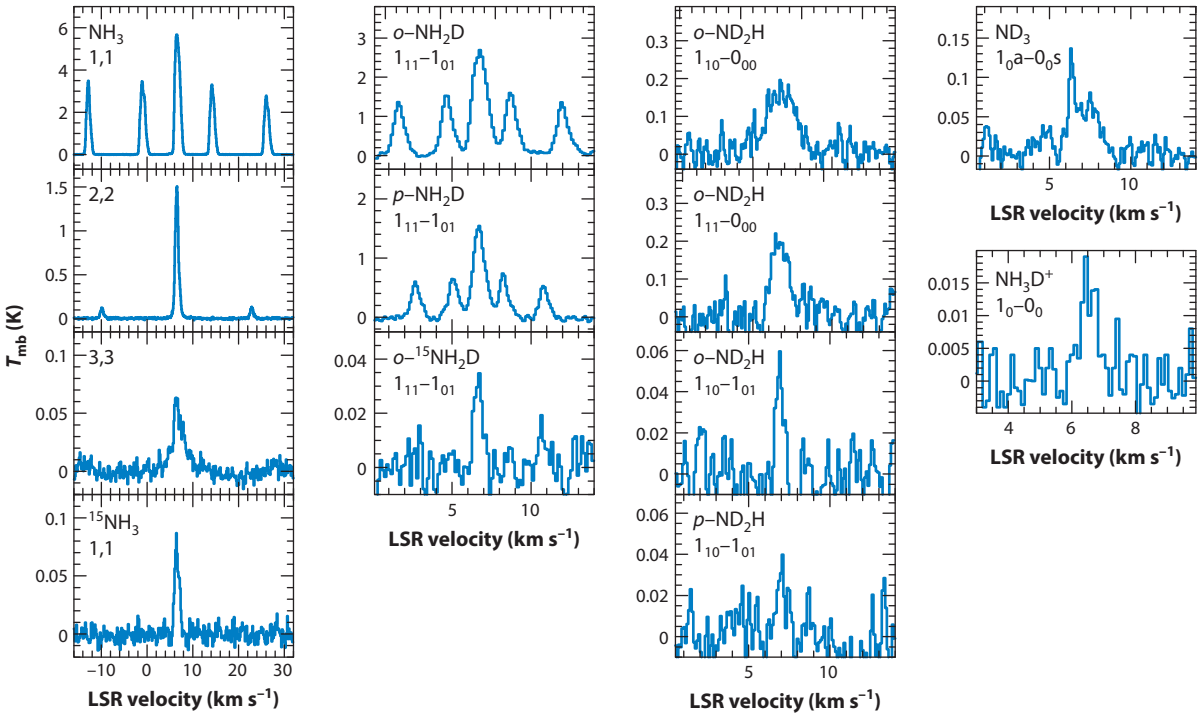

Figure 13

Ground-based spectra of nitrogen hydrides in the protostellar core Barnard 1b [$T = 12$ K, $n_{H_2} = 10^5$ cm^{-3}, $N(H_2) = 10^{23}$cm^{-2}]. Abbreviation: LSR, local standard of rest. This figure has been adapted with permission from Daniel et al. (2013), Lis et al. (2010b), and Cernicharo et al. (2013).

reactions that forms NH_3 favors the formation of *p*-NH_3 owing to spin statistics selection rules (Rist et al. 2013, Faure et al. 2013). This effect could be prominent in cold cores, with predicted OPR ~ 0.5 for NH_3. The deficit in *o*-NH_3 implies a small error in the total NH_3 column density deduced from *p*-NH_3 observations. The amidogen radical NH_2 is formed in the same chain of gas-phase reactions as ammonia. With two identical protons, NH_2 has two spin symmetry states, the *ortho* state with a spin multiplicity of three, which is the most stable, and the *para* state with a spin multiplicity of one, with an energy difference of 30 K. As for ammonia, the NH_2 OPR is sensitive to the presence of an excess of *p*-H_2 and can reach values lower than three, which are not permitted in thermal equilibrium, in *p*-H_2 enriched gas (Le Gal et al. 2014). So far only a handful of measurements of the NH_3 and NH_2 OPRs are available (Persson et al. 2016). Such measurements may be able to put constraints on the H_2 OPR in dense and shielded gas.

Ammonia is a good tracer of both prestellar and protostellar cores, with a fractional abundance relative to H_2 of $\sim 10^{-8}$ (Bergin & Tafalla 2007). It remains undepleted in the gas phase up to relatively large densities $\sim 10^6$ cm^{-3}, in contrast to the case of CO. As illustrated in **Figure 13**, all deuterated ammonia isotopologues have been detected in the ISM: NH_2D, ND_2H, and ND_3 (Roueff et al. 2005), as well as the ^{15}N variants $^{15}NH_3$ (e.g., Lis et al. 2010b) and $^{15}NH_2D$ (Gerin et al. 2009), and even NH_3D^+ (Cernicharo et al. 2013). The deuterated ammonia isotopologues are better tracers of the cold inner regions of prestellar cores, where most molecules are frozen onto grains, than is NH_3 itself, with fractionation levels above 10% in such regions (e.g., Daniel

et al. 2013). The fractionation of ammonia and its precursors NH and NH_2 is most efficient at temperatures lower than ~20 K because it involves reactions with HD, H_2D^+, D_2H^+ and D_3^+ that are enhanced at temperatures below 20 K (Roueff et al. 2015). ND has been detected (Bacmann et al. 2010), with [ND]/[NH] reaching ~10%, a value similar to that observed for $[NH_2D]/[NH_3]$, but with a large uncertainty because of the difference in excitation between NH and ND.

At low temperatures, nitrogen may become fractionated, leading to a possible difference between the elemental isotopic ratio $^{15}N/^{14}N$ and the abundance ratio of nitrogen-bearing species. The topic is of interest because analysis of primitive solar system material as found in carbonaceous chondrites or in micrometeorites has led to the identification of specific regions with isotopic ratios very different from the bulk, in D/H, $^{15}N/^{14}N$, or both (Aléon 2010). The difference between the $^{15}N/^{14}N$ isotopic ratio in the Sun (and the solar system), 2.3×10^{-3}, and the Earth, 3.8×10^{-3}, also indicates that active fractionation processes were operating in the early solar system. Following the evolution of D/H and $^{15}N/^{14}N$ in interstellar molecules along the formation of a protostar and its circumstellar disk is therefore a means of constraining the chemical evolution of the star-forming system and the formation of its primitive bodies. So far, measuring the $^{15}N/^{14}N$ isotopic ratio has proven to be much more difficult than D/H because of the large dynamical range required. Chemical models have investigated the coupled fractionation of hydrogen, carbon, and nitrogen, and also the dependence with time during the collapse. The prediction is that NH_3 should preserve to within 20% the original nitrogen isotopic ratio, unlike other species such as HCN which could become highly fractionated (Wirström et al. 2012, Roueff et al. 2015). Selective photodissociation of N_2, as modeled by Heays et al. (2014), also plays a role in the nitrogen fractionation in protoplanetary disks.

6.4. Sulfur and Other Heavy Element Hydrides

Hydrogen sulfide, H_2S, is the main sulfur hydride in dense clouds, whereas SH and SH^+ are more confined to diffuse and translucent clouds (Crockett et al. 2014, Neufeld et al. 2015b) or the UV-illuminated cloud edges described in Section 4. The sulfur chemistry proceeds differently from that of oxygen or carbon because the hydrogen abstraction reactions between HS_n^+ and H_2 are highly endothermic. The hydrogenation of sulfur atoms on grains, followed by desorption, is a possible chemical pathway to form hydrogen sulfide in dense cores, although no confirmed detection of H_2S ice has been reported so far. Singly and doubly deuterated hydrogen sulfide have been detected in a few dark clouds (van Dishoeck et al. 1995, Vastel et al. 2003), with a significant fractionation level of ~10%. The fractionation is sensitive to the temperature because HDS and D_2S are not detected in hot cores, despite their large H_2S column densities. For the Orion-KL region, the upper limit for the HDS/H_2S ratio is a few $\times 10^{-3}$, at the same level as HDO/H_2O (Crockett et al. 2014).

The halogen hydrides HF and HCl are expected to be the main gas-phase reservoirs of fluorine and chlorine in dense and well-shielded gas (Neufeld & Wolfire 2009) and could be used to monitor the depletion of these elements. The detection of the $J = 2-1$ line of HF in absorption toward SgrB2 (Neufeld et al. 1997) implied a fluorine depletion close to two orders of magnitude relative to its elemental abundance. Surveys of HCl also conclude that chlorine depletes on grains by at least two orders of magnitude (e.g., Peng et al. 2010, Kama et al. 2015). Although many previous analyses relied on collisional cross sections with He, new calculations have been performed for the H_2-HCl system by Lanza et al. (2014), providing further confirmation of the low HCl abundance in dense gas. HCl may return to the gas phase in the hot inner region around massive protostars (Goto et al. 2013).

7. HYDRIDES AS DIAGNOSTIC TOOLS

Because the chemical pathways leading to the formation of interstellar hydrides are relatively simple and well understood, the analysis of the observed abundances is relatively straightforward and provides key information about the physical and chemical conditions within the environments in which hydrides are found. Several examples have already been discussed, including observations of CH^+ and SH^+ in diffuse molecular clouds, which trace the effects of shocks or TDRs (Section 5), and observations of neutral hydrides such as HF, HCl and H_2O in dense clouds, which probe the depletion of heavy elements onto icy grain mantles (Sections 2 and 6). In this section, we discuss several additional cases in which observations of hydride molecules provide unique information about the ISM. In particular, we consider how observations of specific hydrides—namely CH, H_2O, and HF—provide valuable surrogate tracers for molecular hydrogen, the dominant molecular constituent of the ISM but one that is difficult to observe directly, while several hydride cations (including ArH^+, HCl^+, OH^+ and H_2O^+) are most abundant in partially molecular gas, with each molecule predicted to show a peak abundance in material with a specific molecular fraction f_{H_2}. We also discuss how hydride molecules can measure the CR (or X-ray) ionization rate in the Milky Way and other galaxies.

7.1. Hydrides as Tracers of H_2

Although it is the primary molecular constituent of the ISM, H_2 is hard to detect because it lacks a permanent dipole moment. Absorption line observations of the UV (and dipole-allowed) Lyman and Werner bands of H_2 measure the H_2 column density directly, although they are limited to relatively unreddened lines of sight toward relatively nearby hot stars (e.g., Rachford et al. 2009). Absorption in the NIR quadrupole-allowed vibrational bands has also been observed toward a few highly embedded IR sources (Lacy et al. 1994, Kulesa 2002), but is an extremely insensitive probe (in that very large H_2 column densities are needed to generate even very small optical depths). There has, therefore, been a considerable effort to identify surrogate observational tracers that can be used to measure H_2 column densities and masses. Observations of CO emission have been widely used to measure H_2 masses (Bolatto et al. 2013 and references therein) but fail to trace a significant component of the molecular ISM. This component has been called the CO-dark or CO-faint molecular gas (Grenier et al. 2005, Wolfire et al. 2010, Bolatto et al. 2013) and consists of material that is sufficiently shielded from UV radiation to have a substantial H_2 fraction but not so well shielded as to contain abundant CO. This material lies at the transition between diffuse and translucent clouds near $A_V = 1$ mag (e.g., van Dishoeck 1998).

Three hydride molecules—CH, H_2O, and HF—exhibit remarkably constant abundance ratios relative to H_2 and are therefore valuable as surrogate tracers that are sensitive to CO-dark gas. The best-studied case is CH, for which optical absorption-line observations can be calibrated with respect to UV absorption-line observations of H_2, yielding N(CH) and $N(H_2)$ column densities for sight lines with $N(H_2)$ in the range $\sim 10^{19}$–10^{21} cm^{-2} (e.g., Sheffer et al. 2008). The observed $N(CH)/N(H_2)$ ratio has a mean of 3.5×10^{-8}, shows a dispersion of 0.21 dex, and exhibits no dependence on $N(H_2)$; moreover, the $N(CH)/N(H_2)$ ratio can be determined for sight lines of even larger $N(H_2)$—albeit less directly, through a comparison of centimeter-wavelength CH emission with reddening measurements—and is found to remain entirely consistent with the $N(H_2) \lesssim 10^{21}$ cm^{-2} value for H_2 column densities up to $\sim 4 \times 10^{21}$ cm^{-2} (Mattila 1986, Liszt & Lucas 2002). State-of-the-art steady-state chemical models reproduce the observed trend between CH and H_2 correctly for densities larger than 100 cm^{-3}, and for lower densities, the CH production is closely related to that of CH^+, as explained in Section 5.

Observations of submillimeter absorption, performed with *Herschel*-HIFI, have extended the use of hydrides as probes of $N(H_2)$, providing access to the $N = 1, J = 3/2 \rightarrow 1/2$ CH Λ-doublet at 532/536 GHz, along with rotational transitions out of the ground state of the neutral hydrides HF and H_2O. Such observations show the $N(HF)/N(CH)$ ratio to be remarkably constant in diffuse clouds, with a typical value of 0.4, implying a mean $N(HF)/N(H_2)$ ratio of 1.4×10^{-8}, given a $N(CH)/N(H_2)$ ratio of 3.5×10^{-8}. In the limit where $f_{H_2} \sim 1$, this $N(HF)/N(H_2)$ ratio implies that HF accounts for ~40% of the gas-phase fluorine. A direct measurement of the $N(HF)/N(H_2)$ column density ratio in the diffuse ISM has been obtained (Indriolo et al. 2013) toward a single source, the hot star HD 154368, by combining observations of the NIR $v = 1-0$ $R(0)$ HF vibrational transition with those of dipole-allowed UV transitions of H_2. This measurement provided an independent and entirely consistent ($1.15 \pm 0.41 \times 10^{-8}$) determination of the $N(HF)/N(H_2)$ ratio. Originally, the predictions of astrochemical models by Neufeld & Wolfire (2009) for fluorine-bearing interstellar molecules predicted a $N(HF)/N(H_2)$ ratio roughly twice as large as the observed value. However, recent laboratory measurements (Tizniti et al. 2014) of the rate coefficient for the reaction of H_2 with F to form HF appear to have revealed the source of the discrepancy: The original astrochemical models adopted a theoretical value for the rate coefficient at low temperature that was a significant overestimate. Revised models that assume the laboratory-measured value for the rate of HF formation predict $N(HF)/N(H_2)$ ratios in good agreement with the astronomical observations.

Another neutral hydride that has been extensively observed with *Herschel*, H_2O, is a third potential H_2 tracer within the diffuse ISM. The mean $N(H_2O)/N(HF)$ ratio determined from *Herschel* observations of the diffuse ISM is 1.73 (Sonnentrucker et al. 2015), and the standard deviation is 0.87, implying a typical $N(H_2O)/N(H_2)$ ratio of 2.4×10^{-8}. The variation in the H_2O abundance is apparently somewhat larger than those in the CH and HF abundances.

Taken together, submillimeter absorption-line observations of CH, H_2O, and HF provide a valuable tool set for the determination of $N(H_2)$. Their column densities lie in the average ratio $N(CH):N(H_2O):N(HF) = 2.5:1.7:1.0$. For the spectral lines that have been most extensively observed in absorption—the 536 GHz, $N = 1, J = 3/2 \rightarrow 1/2$ transition of CH, the 1113 GHz $1_{11}-0_{00}$ transition of p-H_2O, and the 1232 GHz $J = 1-0$ transition of HF—the corresponding ratio of velocity-integrated optical depths is 0.26:0.6:1.0. Thus, the HF transition provides the most sensitive probe of H_2 along any sight line, followed by H_2O and CH. These probes are complementary because in cases where the HF absorption is optically thick, yielding only a lower limit on the column density, the CH absorption is often optically thin. Conversely, absorption features that are too weak to detect in observations of CH may be detectable in observations of HF. Although CH, HF and H_2O, can be regarded as primary tracers of molecular hydrogen, their column densities are well correlated with other nonhydride molecules that can be detected from the ground at millimeter wavelengths, including HCO^+ (e.g., Lucas & Liszt 1996) and C_2H (Lucas & Liszt 2000, Gerin et al. 2010b). Absorption line observations of these nonhydride secondary tracers can also be used to estimate $N(H_2)$, albeit with lower accuracy. OH can be added to the list of the secondary tracers, given the excellent correlation between the opacities of the HCO^+ $J = 1 \rightarrow 0$ and OH 1665 and 1667 MHz absorption lines (Liszt & Lucas 1996), and the moderate scatter in the OH/H_2O column density ratio (Wiesemeyer et al. 2016).

Along with absorption-line observations of CH, HF, and H_2O, observations of CH and OH emission show considerable promise as a probe of CO-dark molecular gas (Liszt & Lucas 1996). This promise has been demonstrated recently by Allen et al. (2015), who performed a sparse, high-sensitivity pilot survey near the Galactic plane for the 18 cm emission lines of OH: Fewer than one-half of the multiple spectral features thereby detected were accompanied by detectable

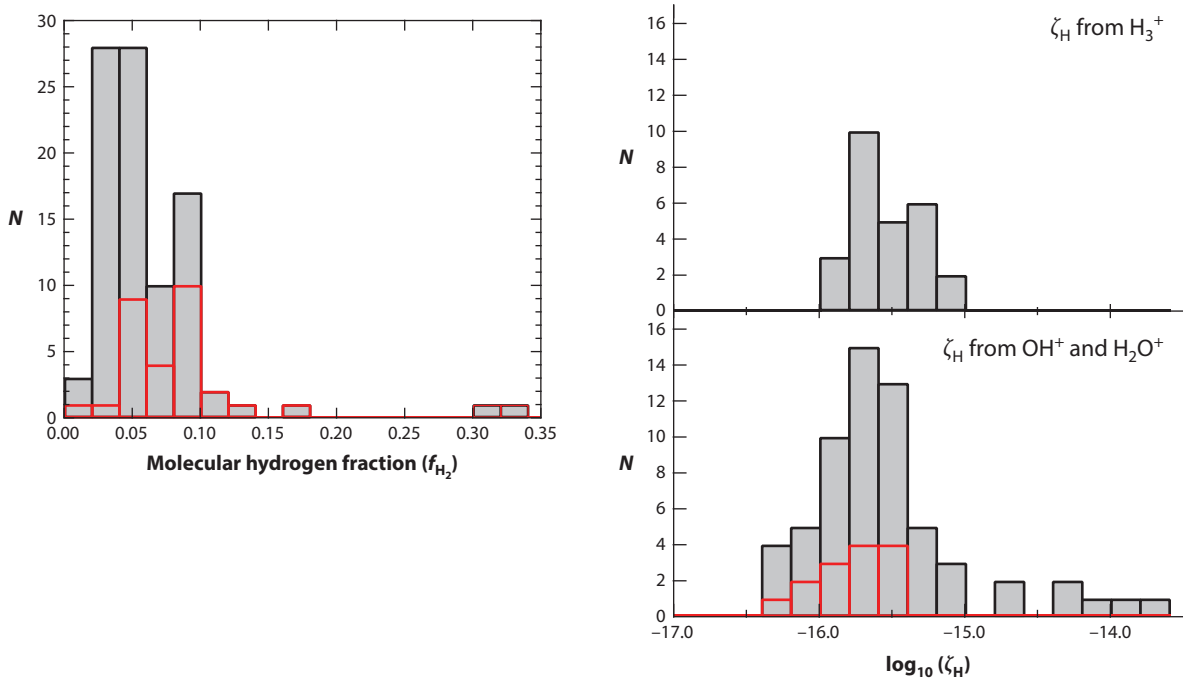

Figure 14

Distributions of molecular hydrogen fraction, f_{H_2} (*left panel*) and cosmic-ray ionization rate, ζ_H (*lower right panel*), inferred from *Herschel Space Observatory* observations of OH^+ and H_2O^+. The red histogram applies to material with line-of-sight velocities within 5 km s^{-1} of the systemic velocity of the background source (i.e., to material that may be in the vicinity of the continuum source). The upper right panel shows the distribution of cosmic-ray ionization rates inferred (for a different set of sight lines) from observations of H_3^+. Adapted from Indriolo et al. (2015) with permission from the AAS.

CO line emission. Further investigations, both observational and theoretical, will be needed to make quantitative use of this H_2 tracer.

7.2. Probes of the Molecular Fraction

Whereas the neutral hydrides CH, HF, and H_2O are most abundant in gas with a large f_{H_2}, several molecular ions show peak abundances in material with a smaller f_{H_2}. This behavior is particularly notable for ions that are destroyed rapidly by reaction with H_2; these include ArH^+, which is destroyed by proton transfer to H_2 (Schilke et al. 2014), and OH^+ and H_2O^+, which undergo H-atom abstraction reactions to form H_2O^+ and H_3O^+ respectively. The $n(OH^+)/n(H_2O^+)$ ratio is a particularly valuable probe of the H_2 fraction (Neufeld et al. 2010) because the reaction of H_2 with OH^+, which forms H_2O^+, competes with dissociative recombination of OH^+ with electrons; thus, the $n(OH^+)/n(H_2O^+)$ ratio is larger in regions of small f_{H_2} and smaller in regions of large f_{H_2}. Through an analysis of 92 OH^+ and H_2O^+ absorption features detected by *Herschel* along the sight lines to 20 bright Galactic continuum sources, Indriolo et al. (2015) obtained the histogram of f_{H_2} values reproduced in **Figure 14** (left panel). This analysis clearly reveals a substantial amount of interstellar gas with a molecular hydrogen fraction of a few percent. Of course, because the observations measure a ratio of column densities rather than volume densities [i.e., $N(OH^+)/N(H_2O^+)$ rather than $n(OH^+)/n(H_2O^+)$], the f_{H_2} values derived are

really averages over the material that contributes most to the OH^+ and H_2O^+ absorption. These f_{H_2} values may therefore differ substantially from those derived for the entire sight line from a comparison of $N(H_2)$ and $N(H)$.

The argonium ion, ArH^+, traces material of even smaller f_{H_2}. Because the dissociative recombination of ArH^+ is unusually slow, reactions with H_2 become the dominant destruction mechanism for $f_{H_2} \gtrsim 10^{-4}$, and the ArH^+ abundance starts to drop once f_{H_2} increases beyond that value. Thus, as discussed by Schilke et al. (2014), ArH^+ serves as a unique probe of material that is almost purely atomic. This prediction for the behavior of ArH^+ is supported by the observational finding that the distribution of ArH^+ is entirely different from that of the other interstellar hydrides (see **Figures 6** and **7** in Section 3).

7.3. Probes of the Cosmic-Ray Ionization Rate

Unlike the formation of CH^+ and SH^+, which is driven by shocks or turbulent dissipation or is enhanced in strongly FUV-irradiated gas, the formation of ArH^+, OH^+, and H_2O^+ is initiated by CRs. ArH^+ formation is driven by the CR ionization of atomic argon, which then reacts with H_2 to form ArH^+; in the case of OH^+ and H_2O^+ formation, the CR ionization of H (or H_2, in material of large f_{H_2}) is the process that initiates the relevant reaction chain. Observations of the abundances of OH^+ and H_2O^+ in diffuse clouds, supported by detailed astrochemical calculations (Hollenbach et al. 2012), have been used to measure the CR ionization rate in the Milky Way (Gerin et al. 2010a, Neufeld et al. 2010, Indriolo et al. 2015).

Indriolo et al. (2015) performed an analysis of all the relevant data available from *Herschel* to obtain the histogram reproduced in **Figure 14** (lower right panel), which shows the distribution of CR ionization rates in the disk of the Milky Way, ζ_H, defined here as the total rate of ionization per H atom. This quantity shows a log-normal distribution, with $\log_{10}(\zeta_H)$ having a mean of -15.75 (corresponding to $\zeta_H = 1.8 \times 10^{-16}\ s^{-1}$) and standard deviation of 0.29. The results for ζ_H obtained from OH^+ and H_2O^+ are considerably larger than the canonical values adopted for diffuse clouds by most authors prior to 2002 but are in good agreement with estimates (e.g., Indriolo & McCall 2012) derived (for different sight lines) from mid-IR observations of H_3^+. The upper right panel in **Figure 14** shows the distribution of ζ_H derived from recent H_3^+ observations.

The ionization rates inferred for material in the Galactic Center are typically 10–100 times as large as the average value inferred for gas in the disk, and even larger ionization rates (exceeding $10^{-13}\ s^{-1}$) have been derived for circumnuclear regions within the ULIRGs (ultraluminous infrared galaxies) Arp 220 and NGC 4418 (González-Alfonso et al. 2013). Because ionization by hard X-rays has similar effects on the chemistry to those of CR ionization, it is not possible to unambiguously discriminate between these two possible ionization sources based on observations of hydrides alone.

7.4. Other Diagnostic Uses

In addition to diagnostics enabled by an understanding of hydride chemistry, observations of hydrides offer other tools that measure key parameters of the interstellar environment. The oblate symmetric top molecules NH_3 and H_3O^+ can provide physical probes of the gas temperature. For these molecules, the lowest states of a given quantum number K are metastable (and have a total angular momentum quantum number $J = K$). These metastable states do not undergo radiative decay, and thus their relative populations are determined by nonradiative processes. For low-lying metastable states of NH_3 and H_3O^+, the relative populations are determined by collisional excitation and probe the kinetic temperature of the gas, providing a sort of molecular cloud

thermometer (e.g., Walmsley & Ungerechts 1983). In the case of high-lying metastable states, however, the effects of formation pumping may complicate the interpretation of the observations (e.g., Lis et al. 2014).

The Zeeman splitting of hydride spectral lines offers another important diagnostic tool that has been used to estimate the interstellar magnetic field strength. The paramagnetic OH radical is particularly valuable, and absorption line observations of its 18-cm transitions have been used to determine the magnetic field in interstellar gas with densities in the range $n_H \sim 10^2$–10^4 cm^{-3} (e.g., the review of Crutcher 2012). This material is intermediate between the lower-density gas probed by HI Zeeman measurements and the higher-density gas probed by CN Zeeman measurements. At even higher densities, the Zeeman splitting of OH and H_2O maser transitions has been used to measure magnetic field strengths, revealing fields in excess of 100 mG in some extreme cases.

Because the 22-GHz water maser emissions from shocked regions can be extraordinarily bright, they may be observed by means of very long baseline interferometry, providing sub-milliarcsecond resolution and the possibility of measuring parallaxes and proper motions with accuracies of ~10 μas and ~100 μas year^{-1}, respectively (e.g., Reid et al. 2009, Honma et al. 2012). Such measurements provide uniquely valuable probes of fundamental Galactic parameters such as the distance to the Galactic Center and the circular rotation speed at the solar circle.

Finally, observations of hydride isotopologues can be used to determine elemental isotope ratios, which in turn can provide constraints on star formation history and chemical evolution. In the diffuse ISM, for example, where fractionation is generally believed to be unimportant for isotopes of elements other than hydrogen or carbon, observations of $H_2^{35}Cl^+$ and $H_2^{37}Cl^+$ have been used to determine the $^{35}Cl/^{37}Cl$ isotopic ratio, both in the Galactic disk (Neufeld et al. 2015a and references therein) and in the absorber at a redshift of 0.89 in front of the lensed blazar PKS 1830-211 (Muller et al. 2014a; see Section 8). All these determinations are entirely consistent with the solar system $^{35}Cl/^{37}Cl$ isotopic ratio of 3.1 (Lodders 2003).

8. HYDRIDES IN EXTERNAL GALAXIES

As relatively abundant and ubiquitous species, hydrides are detected in external galaxies, from local objects up to high-redshift systems. The list of detected species includes water vapor (Yang et al. 2013, Omont et al. 2013), OH, and the related ions H_3O^+, H_2O^+, and OH^+; NH_3, CH, and CH^+, as well as HF and the chlorine bearing species HCl and H_2Cl^+ (van der Werf et al. 2010; Rangwala et al. 2011, 2014; González-Alfonso et al. 2012, 2013; Kamenetzky et al. 2012; Muller et al. 2014a,b). The hydride diagnostic capabilities discussed in Section 7 can be exploited to probe the physical conditions, turbulence, and radiation field, including X-rays and CRs, in a more extreme range than what is found in the Milky Way.

8.1. Local Galaxies

FIR spectroscopy, performed first with ISO and then with *Herschel*, revealed a diversity of spectral lines, especially from the hydrides listed above that accompany the set of CO rotational lines and atomic fine structure lines. In local galaxies (with redshift $z < 0.1$), the strongest rotational lines of water vapor are the $2_{02} - 1_{11}$ and $3_{21} - 3_{12}$ transitions with rest frequencies 987.9 and 1162.9 GHz. Their luminosities are linearly correlated with the FIR luminosity, L_{FIR}, across a broad range of IR luminosities, 1–300 × 10^{10} $L_\odot$ (i.e., from normal galaxies up to very active starbursts) (Yang et al. 2013). Radiative transfer models show that FIR pumping is an important source of excitation for most H_2O lines, except for those connected to the *ortho* or *para* ground states. Fully resolved line profiles have been obtained with HIFI and show the complexity of the line profiles even in

nearby galaxies: Toward M82, different H_2O lines have different line profiles ranging from pure absorption to pure emission (Weiß et al. 2010).

Active galactic nucleus (AGN): a compact region, located near the center of a galaxy, that emits intense radiation as the result of the accretion of matter onto a supermassive black hole

Starburst galaxy: a galaxy forming stars at a rate of up to 10^3 $M_\odot$ yr^{-1}, which is much higher than the average of a few $M_\odot$ yr^{-1}

XDR: X-ray dominated region

At moderate spectral resolution (~200 km s^{-1}), submillimeter and FIR hydride lines appear in emission, in absorption, or even with P-Cygni profiles. In galaxies hosting a compact starburst or an active galactic nucleus (AGN), the FIR radiation from the hot dust pumps the rotational levels, leading to a variety of line profiles that reveal the conditions close to the heavily buried compact source (van der Werf et al. 2010). OH lines from excited levels are especially interesting because they trace powerful outflows of molecular material (Sturm et al. 2011, González-Alfonso et al. 2012) that represent an important source of negative feedback in starburst galaxies or AGNs. In an analysis of 29 galaxies, González-Alfonso et al. (2015) clearly show that the OH 65-μm line doublet equivalent width probes the fraction of IR luminosity produced by a compact, warm source (i.e., this equivalent width is closely related to the presence of an heavily buried active region that could escape detection otherwise). Absorption from excited levels of other hydrides such as water vapor, OH^+, and H_2O^+ can also be detected in the FIR/submillimeter range. H_3O^+ deserves special treatment. Toward the compact IR galaxies Arp 220 and NGC 4418, absorption from H_3O^+ lines tracing the metastable levels of this symmetric top molecule is detected up to energies of ~1300 K. In the Galactic sources SgrB2 and W31C, these lines trace the formation process of H_3O^+ and can therefore be used to accurately infer the ionization rate, which reaches $\zeta_H > 10^{-13}$ s^{-1} in both NGC 4418 and Arp 220, as compared with the mean value in the Galactic disk of $\zeta_H = 2 \times 10^{-16}$ s^{-1} (Indriolo et al. 2015). Non-metastable lines of H_3O^+ are accessible from the ground, the strongest being the $3_2^+ - 2_2^+$ line at 364 GHz (Aalto et al. 2011).

In external galaxies, hydrides are important probes of the diffuse clouds that do not radiate in CO. For instance, Appleton et al. (2013) report the detection of water vapor in the large shock of Stephan's Quintet, a group of five interacting galaxies. The ground state p-H_2O transition is the brightest submillimeter emission line detected in this system, excluding the FIR structure lines [CII] at 158 μm and [OI] at 63 μm. The current generation of high-resolution spectrometers operating at visible wavelengths allows measurement of CH, CH^+, and CN absorption lines toward stars in nearby galaxies. In the Magellanic Clouds, the relationships between CN, CH, CH^+, NaI, and KaI are generally consistent with those of the Milky Way, but the overall CH abundance relative to H_2 is more variable, likely because of the broad range of physical conditions encountered along such sight lines and the lower carbon abundance of the Magellanic Clouds compared to the Milky Way (Welty et al. 2006). The supernova SN2014J in M82 (Ritchey et al. 2015) provided a bright enough background target to probe the ISM properties in the Galaxy and in M82 along this sight line. The enhanced CH^+/CH ratio may indicate an enhanced level of turbulence in this actively star-forming galaxy.

8.2. Active Galactic Nuclei: X-Ray Dominated Region Prototypes

When molecular gas is exposed to intense X-ray radiation, a specific chemistry can develop. As compared with PDRs, X-ray dominated regions (XDRs) show longer columns of warm molecular gas because X-rays can penetrate longer columns than UV photons. Because of the increased ionization rate due to X-rays and the higher gas temperature in XDRs, some molecular abundances differ from those in PDRs, particularly the oxygen hydrides OH^+, H_2O^+, and H_3O^+. In dense gas illuminated by X-rays, these species are predicted to present strong emission features because the high electron density causes increased excitation. The close environment of the supermassive accreting black hole in an AGN can be considered an XDR, even though some active galaxies also host starbursts. XDRs also exist in the close vicinity of protostars and have been modeled, for example, by Stäuber et al. (2005). The *Herschel*-SPIRE (Spectral and Photometric Imaging

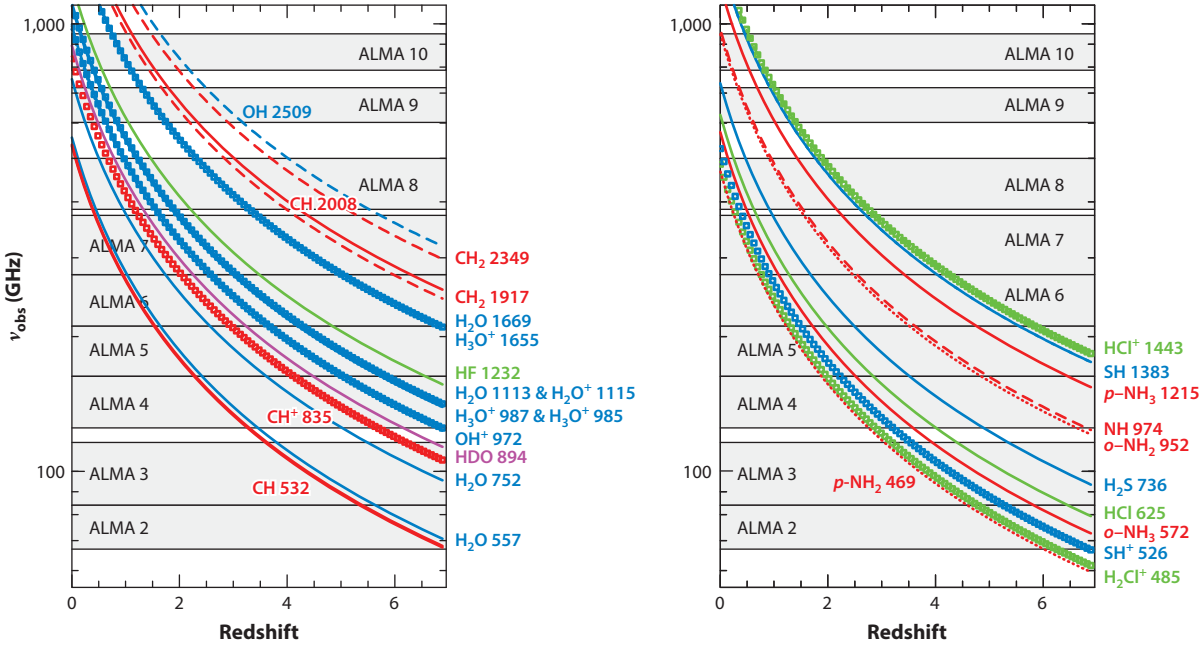

Figure 15

Frequencies of the ground state transitions of the main hydrides as a function of redshift. Some rotationally excited lines of water vapor are also included. Molecular ions are shown with squares. In the left panel, oxygen-bearing species are displayed in blue, carbon-bearing species in red, and halogens in green. On the right panel, nitrogen-bearing species are shown in red, sulfur-bearing species in blue, and halogens in green. ALMA bands 2–10 are indicated in gray.

Receiver) spectrum of Mrk 231, an AGN template, shows prominent OH^+ and H_2O^+ rotational lines in emission (van der Werf et al. 2010). Other species sensitive to high X-ray irradiation are atomic carbon, H_3^+, H_2O, and HCN. Because S^{2+} reacts rapidly with H_2, producing SH^+ and other species, Abel et al. (2008) have proposed that SH^+ could be an excellent XDR tracer. This work remains qualitative because the reaction branching ratio toward SH^+ is not known; a further exploration of the reactivity of doubly ionized ions with H_2 (e.g., C^{2+}) and of the branching ratios toward hydrides is needed to support this potential chemical route.

8.3. High-Redshift Galaxies

Hydride lines at terahertz rest frequencies are redshifted into the (sub)millimeter range and become accessible to the ALMA and NOEMA (the Northern Extended Millimeter Array) interferometers, offering new diagnostic capabilities of the conditions in high-redshift galaxies. **Figure 15** shows the ground-state hydride lines accessible to ALMA with the corresponding redshift range. For water vapor, excited lines should be easy to detect (Omont et al. 2013), with line strength only a factor of two to three lower than that of CO. Nevertheless, the detection of water vapor at high redshift was achieved about two decades after that of CO, largely because the limited bandwidth of available receivers prohibited searching over a broad frequency range. Because the CO rotational line frequencies are relatively distant from the strongest H_2O line frequencies, targeting CO meant avoiding H_2O until recently. The tight correlation of the H_2O line luminosity with the FIR luminosity may be used to derive the star formation rate.

James Webb Space Telescope (JWST): a 6.5-m telescope, operating between 0.6 and 28 μm, expected to be launched in late 2018

On sight lines toward gravitationally lensed quasi-stellar objects (QSOs), the gas of the lensing galaxy may produce absorption lines on the continuum of the background object. The sight line toward the radio-loud QSO PKS1830-211 is particularly rich, with numerous absorption lines detected toward the two main images, sampling two lines of sight in the lensing galaxy at $z = 0.89$. ALMA observations enabled the detection of the same hydride lines that were seen in the Milky Way by *Herschel* (Muller et al. 2014a,b). Other high-redshift hydride detections include H_2O^+ in a bright submillimeter galaxy (Weiß et al. 2013), CH in the average spectrum of 22 such objects (Spilker et al. 2014), and CH^+ in the optical afterglow spectrum of the gamma ray burst GRB 145050A at $z = 0.89$ (Fynbo et al. 2014) and in three hyperluminous galaxies (Falgarone et al. 2015).

Although the same species are detected at $z \sim 1$ as in the Milky Way, some hydrides may become undetectable at higher redshift because of the lack of the corresponding chemical element. For instance, HF has been tentatively detected in the Cloverleaf QSO at $z = 2.56$ (Monje et al. 2011) but not in the higher-redshift source APM 08279 + 5255 at $z = 3.89$ (Lis et al. 2011). The absence of HF is best explained by a low fluorine abundance, because the same source exhibits bright CO and H_2O lines.

The comparison of carefully selected hydride line profiles provides an interesting test of the variation of two fundamental constants with time, the fine structure constant $\alpha = e^2/\hbar c$ and the proton-to-electron mass ratio $\mu = m_p/m_e$. The sensitivity of the CH doublet at 532/536 GHz to variations in α and μ has been computed by de Nijs et al. (2012). These lines can be observed simultaneously with the $1_{10} - 1_{01}$ transition of o-H_2O, reducing the systematic effects when comparing lines at very different frequencies, and therefore are complementary to other diagnostics such as NH_3, CH_3OH, and H_2 (discussed by Jansen et al. 2014).

9. CONCLUSIONS AND FUTURE PROSPECTS

Since their first discovery in the diffuse ISM, hydrides have been proven to exist in a wide variety of interstellar and circumstellar environments, from the most diffuse, almost purely atomic regions, up to dense cores and protoplanetary disks. Given the relative simplicity of their chemistry and their well-understood formation processes, the diagnostic properties of hydrides need to be further explored in the future by taking advantage of the increasing capabilities of high-spectral-resolution spectrometers from the UV-visible range up to centimeter wavelengths. Although hydride ground-state transitions at $z = 0$ are mostly unobservable from ground-based observatories, in distant galaxies they are redshifted to spectral regions with better atmospheric transmission that can be observed by ALMA and NOEMA (**Figure 15**). This enables diagnostics of the presence of molecular hydrogen, the CR ionization rate, and elemental abundances, as well as of dynamical processes in the forms of shocks, turbulence and large scale winds, from the ISM in the Milky Way up to the most distant galaxies. The combined increase in sensitivity and spectral resolution will enable more accurate measurements of isotopic ratios, with a focus on deuterium and nitrogen, to study the origin of volatiles in the solar system, and more generally the formation of planets in circumstellar disks. It will be exciting to connect these observations of the ISM with the measurements performed on the 67P/Churyumov-Gerasimenko comet by the Rosetta spacecraft.

At longer wavelengths, the development of powerful centimeter-wavelength instruments offers interesting possibilities for accessing the Λ-doubling transitions of OH (both in the ground state and in excited levels) and CH, for studying the inversion transitions of NH_3, and for comparing the distribution of these species with that of atomic hydrogen at unprecedented sensitivity and spatial resolution. At shorter wavelengths, the launch of JWST and the construction of the next

generation of ground-based telescopes will provide new tools for studying the relation between ices and gas-phase species, especially water, methane, and associated radicals.

To obtain the best results from these upcoming facilities, several scientific issues in the fields of astrochemistry and molecular physics must be addressed. On the astrophysics side, a significant issue is the understanding of the effects of non-equilibrium processes on the abundance and excitation of the main hydrides. As described above, the production and excitation of a reactive hydride such as CH^+ are affected by the large-scale and small-scale dynamics of the media, their multi-phase structure, and the details of the formation and excitation process. A related topic that must be addressed is the hydride OPR, and how it relates to the H_2 OPR. Doing so will require investigations of the reaction mechanisms that lead to hydride formation and destruction (while taking the spin symmetry states into account), as well as more accurate astronomical observations.

The field of laboratory astrophysics is developing fast. The interplay between the gas phase and the solid phase is a key area for progress. Because hydrides form through hydrogen abstraction reactions, their abundances are particularly sensitive to the dissociative recombination rates of molecular ions. The new cryogenic storage ring in Heidelberg should provide measurements of the dissociative recombination rate of rotationally cold ions such as OH^+. Other exciting developments in laboratory astrophysics include deeper studies of the interaction of ices with FUV and energetic radiation using synchrotron radiation sources, particle bombardment simulating CR irradiation, and advanced theoretical calculations of molecular processes. Close collaborations between molecular physicists and astronomers will remain a key asset in this area, as has been true in the past decades.

DISCLOSURE STATEMENT

The authors are not aware of any affiliations, memberships, funding, or financial holdings that might be perceived as affecting the objectivity of this review.

ACKNOWLEDGMENTS

We thank M. Agúndez, J. Black, B. Godard, D. Hollenbach, N. Indriolo, E. Falgarone, S. Federman, H. Liszt, P. Sonnentrucker, E. Roueff, and M. Wolfire for a critical reading of an early version of the manuscript and our editor E. van Dishoeck for her detailed comments and relevant suggestions. We owe special thanks to M. Agúndez, E. Dartois, B. Godard, F. Levrier, Z. Nagy, and C. Persson for help with the preparation of some figures. The work of D.A.N. has been supported by a grant issued by NASA's Jet Propulsion Laboratory for the analysis of Herschel data and a grant from NASA's Astrophysics Data Analysis Program (ADAP). J.R.G. thanks the Spanish MINECO and the ERC for support under grants AYA2012-32032 and ERC-2013-Syg-610256-NANOCOSMOS. M.G. thanks the INSU CNRS program PCMI, and CNES for support.

LITERATURE CITED

Aalto S, Costagliola F, van der Tak F, Meijerink R. 2011. *Astron. Astrophys.* 527:A69
Abel NP, Federman SR, Stancil PC. 2008. *Astrophys. J. Lett.* 675:L81–84
Agúndez M, Goicoechea JR, Cernicharo J, Faure A, Roueff E. 2010. *Astrophys. J. Lett.* 713:662–70
Alata I, Cruz-Diaz GA, Muñoz Caro GM, Dartois E. 2014. *Astron. Astrophys.* 569:A119
Aleman I, Ueta T, Ladjal D, et al. 2014. *Astron. Astrophys.* 566:A79

Aléon J. 2010. *Astrophys. J.* 722:1342–51
Allen RJ, Hogg DE, Engelke PD. 2015. *Astron. J.* 149:123
Allers KN, Jaffe DT, Lacy JH, Draine BT, Richter MJ. 2005. *Astrophys. J.* 630:368–80
Amano T. 2010. *Astron. Astrophys.* 516:L4
Appleton PN, Guillard P, Boulanger F, et al. 2013. *Astrophys. J.* 777:66
Arasa C, Koning J, Kroes GJ, Walsh C, van Dishoeck EF. 2015. *Astron. Astrophys.* 575:A121
Bacmann A, Caux E, Hily-Blant P, et al. 2010. *Astron. Astrophys.* 521:L42
Barlow MJ, Swinyard BM, Owen PJ, et al. 2013. *Science* 342:1343–45
Bates DR, Spitzer L Jr. 1951. *Astrophys. J.* 113:441–63
Batrla W, Wilson TL. 2003. *Astron. Astrophys.* 408:231–35
Beckman JE, Watt GD, White GJ, et al. 1982. *Mon. Not. R. Astron. Soc.* 201:357–64
Benz AO, Bruderer S, van Dishoeck EF, et al. 2010. *Astron. Astrophys.* 521:L35
Benz AO, Bruderer S, van Dishoeck EF, Stäuber P, Wampfler SF. 2013. *J. Phys. Chem. A* 117:9840–47
Bergin EA, Tafalla M. 2007. *Annu. Rev. Astron. Astrophys.* 45:339–96
Black JH. 1998. *Faraday Discuss.* 109:257–66
Black JH, Dalgarno A. 1976. *Astrophys. J. Lett.* 203:132–42
Black JH, Dalgarno A. 1977. *Astrophys. J. Suppl.* 34:405–23
Black JH, van Dishoeck EF. 1987. *Astrophys. J. Lett.* 322:412–49
Blake GA, Keene J, Phillips TG. 1985. *Astrophys. J. Lett.* 295:501–6
Bolatto AD, Wolfire M, Leroy AK. 2013. *Annu. Rev. Astron. Astrophys.* 51:207–68
Boogert ACA, Gerakines PA, Whittet DCB. 2015. *Annu. Rev. Astron. Astrophys.* 53:541–81
Boonman AMS, Doty SD, van Dishoeck EF, et al. 2003. *Astron. Astrophys.* 406:937–55
Bottinelli S, Wakelam V, Caux E, et al. 2014. *Mon. Not. R. Astron. Soc.* 441:1964–73
Bron E, Le Bourlot J, Le Petit F. 2014. *Astron. Astrophys.* 569:A100
Bruderer S, Benz AO, Stäuber P, Doty SD. 2010. *Astrophys. J. Lett.* 720:1432–53
Butner HM, Charnley SB, Ceccarelli C, et al. 2007. *Astrophys. J. Lett. Lett.* 659:L137–40
Carr JS, Najita JR. 2008. *Science* 319:1504–6
Carruthers GR. 1970. *Astrophys. J. Lett. Lett.* 161:L81–85
Caselli P, Ceccarelli C. 2012. *Astron. Astrophys. Rev.* 20:56
Caselli P, Keto E, Bergin EA, et al. 2012. *Astrophys. J. Lett.* 759:L37
Cazaux S, Tielens AGGM. 2004. *Astrophys. J. Lett.* 604:222–37
Cernicharo J, Liu XW, González-Alfonso E, et al. 1997. *Astrophys. J. Lett.* 483:L65–68
Cernicharo J, Tercero B, Fuente A, et al. 2013. *Astrophys. J. Lett.* 771:L10
Chastain RJ, Cotten D, Magnani L. 2010. *Astron. J.* 139:267–78
Chernoff DF, McKee CF, Hollenbach DJ. 1982. *Astrophys. J. Lett.* 259:L97–101
Cheung AC, Rank DM, Townes CH, Thornton DD, Welch WJ. 1968. *Phys. Rev. Lett.* 21:1701–5
Cheung AC, Rank DM, Townes CH, Thornton DD, Welch WJ. 1969. *Nature* 221:626–28
Choi Y, van der Tak FFS, Bergin EA, Plume R. 2014. *Astron. Astrophys.* 572:L10
Coutens A, Vastel C, Hincelin U, et al. 2014. *Mon. Not. R. Astron. Soc.* 445:1299–313
Crane P, Lambert DL, Sheffer Y. 1995. *Astrophys. J. Suppl.* 99:107
Crockett NR, Bergin EA, Neill JL, et al. 2014. *Astrophys. J. Lett.* 781:114
Crutcher RM. 2012. *Annu. Rev. Astron. Astrophys.* 50:29–63
Daniel F, Dubernet ML, Grosjean A. 2011. *Astron. Astrophys.* 536:A76
Daniel F, Faure A, Dagdigian PJ, et al. 2015. *Mon. Not. R. Astron. Soc.* 446:2312–16
Daniel F, Gérin M, Roueff E, et al. 2013. *Astron. Astrophys.* 560:A3
Dartois E, Cox P, Roelfsema PR, et al. 1998. *Astron. Astrophys.* 338:L21–24
De Luca M, Gupta H, Neufeld D, et al. 2012. *Astrophys. J. Lett.* 751:L37
de Nijs AJ, Ubachs W, Bethlem HL. 2012. *Phys. Rev. A* 86:032501
Douglas AE, Herzberg G. 1941. *Astrophys. J. Lett.* 94:381
Draine BT, Katz N. 1986. *Astrophys. J. Lett.* 310:392–407
Draine BT, McKee CF. 1993. *Annu. Rev. Astron. Astrophys.* 31:373–432
Draine BT, Roberge WG, Dalgarno A. 1983. *Astrophys. J. Lett.* 264:485–507
Dubernet ML, Alexander MH, Ba YA, et al. 2013. *Astron. Astrophys.* 553:A50

Dulieu F, Congiu E, Noble J, et al. 2013. *Sci. Rep.* 3:1338
Eddington AS. 1926. *R. Soc. Lond. Proc. Ser. A* 111:424–56
Elitzur M, Hollenbach DJ, McKee CF. 1989. *Astrophys. J. Lett.* 346:983–90
Ewen HI, Purcell EM. 1951. *Nature* 168:356
Falgarone E, Zwaan M, Godard B, et al. 2015. In *Revolution in Astronomy with ALMA: The Third Year*, ed. D Iono, K Tatematsu, A Wootten, L Testi, pp. 55–60. San Francisco: Astron. Soc. Pac.
Falgarone E, Phillips TG, Pearson JC. 2005. *Astrophys. J. Lett.* 634:L149–52
Faure A, Crimier N, Ceccarelli C, et al. 2007. *Astron. Astrophys.* 472:1029–35
Faure A, Hily-Blant P, Le Gal R, et al. 2013. *Astrophys. J. Lett.* 770:L2
Fedele D, Bruderer S, van Dishoeck EF, et al. 2013. *Astron. Astrophys.* 559:A77
Federman SR, Cardell JA, van Dishoeck EF, Lambert DL, Black JH. 1995. *Astrophys. J. Lett.* 445:325–29
Fedoseev G, Ioppolo S, Linnartz H. 2015. *Mon. Not. R. Astron. Soc.* 446:449–58
Feuchtgruber H, Helmich FP, van Dishoeck EF, Wright CM. 2000. *Astrophys. J. Lett.* 535:L111–14
Field GB, Somerville WB, Dressler K. 1966. *Annu. Rev. Astron. Astrophys.* 4:207–44
Flagey N, Goldsmith PF, Lis DC, et al. 2013. *Astrophys. J. Lett.* 762:11
Frail DA, Mitchell GF. 1998. *Astrophys. J. Lett.* 508:690–95
Fynbo JPU, Krühler T, Leighly K, et al. 2014. *Astron. Astrophys.* 572:A12
Geballe TR, Oka T. 1996. *Nature* 384:334–35
Gerin M, De Luca M, Black J, et al. 2010a. *Astron. Astrophys.* 518:L110
Gerin M, De Luca M, Goicoechea JR, et al. 2010b. *Astron. Astrophys.* 521:L16
Gerin M, Levrier F, Falgarone E, et al. 2012. *R. Soc. Lond. Philos. Trans. Ser. A* 370:5174–85
Gerin M, Marcelino N, Biver N, et al. 2009. *Astron. Astrophys.* 498:L9–12
Glover SCO, Mac Low MM. 2007. *Astrophys. J. Lett.* 659:1317–37
Godard B, Cernicharo J. 2013. *Astron. Astrophys.* 550:A8
Godard B, Falgarone E, Gerin M, et al. 2012. *Astron. Astrophys.* 540:A87
Godard B, Falgarone E, Pineau des Forêts G. 2009. *Astron. Astrophys.* 495:847–67
Godard B, Falgarone E, Pineau des Forêts G. 2014. *Astron. Astrophys.* 570:A27
Goddi C, Zhang Q, Moscadelli L. 2015. *Astron. Astrophys.* 573:A108
Goicoechea JR, Chavarría L, Cernicharo J, et al. 2015. *Astrophys. J. Lett.* 799:102
Goicoechea JR, Etxaluze M, Cernicharo J, et al. 2013. *Astrophys. J. Lett.* 769:L13
Goicoechea JR, Joblin C, Contursi A, et al. 2011. *Astron. Astrophys.* 530:L16
Gómez-Carrasco S, Godard B, Lique F, et al. 2014. *Astrophys. J. Lett.* 794:33
González-Alfonso E, Fischer J, Bruderer S, et al. 2013. *Astron. Astrophys.* 550:A25
González-Alfonso E, Fischer J, Graciá-Carpio J, et al. 2012. *Astron. Astrophys.* 541:A4
González-Alfonso E, Fischer J, Sturm E, et al. 2015. *Astrophys. J. Lett.* 800:69
Goto M, Usuda T, Geballe TR, et al. 2013. *Astron. Astrophys.* 558:L5
Gredel R. 1997. *Astron. Astrophys.* 320:929–44
Grenier IA, Casandjian JM, Terrier R. 2005. *Science* 307:1292–95
Gusdorf A, Pineau des Forêts G, Cabrit S, Flower DR. 2008. *Astron. Astrophys.* 490:695–706
Habart E, Dartois E, Abergel A, et al. 2010. *Astron. Astrophys.* 518:L116
Heays AN, Visser R, Gredel R, et al. 2014. *Astron. Astrophys.* 562:A61
Herbst E, Klemperer W. 1973. *Astrophys. J. Lett.* 185:505–34
Hierl PM, Morris RA, Viggiano AA. 1997. *J. Chem. Phys.* 106:10145–52
Hogerheijde MR, Bergin EA, Brinch C, et al. 2011. *Science* 334:338–40
Hollenbach D, Elitzur M, McKee CF. 2013. *Astrophys. J. Lett.* 773:70
Hollenbach D, Kaufman MJ, Bergin EA, Melnick GJ. 2009. *Astrophys. J. Lett.* 690:1497–521
Hollenbach D, Kaufman MJ, Neufeld D, Wolfire M, Goicoechea JR. 2012. *Astrophys. J. Lett.* 754:105
Hollenbach DJ, Tielens AGGM. 1999. *Rev. Mod. Phys.* 71:173–230
Hollenbach DJ, Werner MW, Salpeter EE. 1971. *Astrophys. J. Lett.* 163:165–80
Hollis JM, Jewell PR, Lovas FJ. 1995. *Astrophys. J. Lett.* 438:259–64
Honma M, Nagayama T, Ando K, et al. 2012. *Publ. Astron. Soc. Jpn.* 64:136
Indriolo N, McCall BJ. 2012. *Astrophys. J. Lett.* 745:91
Indriolo N, Neufeld DA, Gerin M, et al. 2015. *Astrophys. J. Lett.* 800:40

Indriolo N, Neufeld DA, Seifahrt A, Richter MJ. 2013. *Astrophys. J. Lett.* 764:188
Indriolo N, Oka T, Geballe TR, McCall BJ. 2010. *Astrophys. J. Lett.* 711:1338–42
Jansen P, Bethlem HL, Ubachs W. 2014. *J. Chem. Phys.* 140:010901
Jiménez-Serra I, Caselli P, Martín-Pintado J, Hartquist TW. 2008. *Astron. Astrophys.* 482:549–59
Kama M, Caux E, López-Sepulcre A, et al. 2015. *Astron. Astrophys.* 574:A107
Kamenetzky J, Glenn J, Rangwala N, et al. 2012. *Astrophys. J. Lett.* 753:70
Karska A, Kristensen LE, van Dishoeck EF, et al. 2014. *Astron. Astrophys.* 572:A9
Kaufman MJ, Neufeld DA. 1996. *Astrophys. J. Lett.* 456:611
Knez C, Lacy JH, Evans NJ II, van Dishoeck EF, Richter MJ. 2009. *Astrophys. J. Lett.* 696:471–83
Kramers HA, Ter Haar D. 1946. *Bull. Astron. Inst. Neth.* 10:137–46
Krełowski J, Beletsky Y, Galazutdinov GA. 2010. *Astrophys. J. Lett.* 719:L20–22
Kulesa CA. 2002. *Molecular hydrogen and its ions in dark interstellar clouds and star forming regions*. PhD thesis, Univ. Ariz.
Lacy JH, Carr JS, Evans NJ II, et al. 1991. *Astrophys. J. Lett.* 376:556–60
Lacy JH, Knacke R, Geballe TR, Tokunaga AT. 1994. *Astrophys. J. Lett.* 428:L69–72
Lanza M, Kalugina Y, Wiesenfeld L, Faure A, Lique F. 2014. *Mon. Not. R. Astron. Soc.* 443:3351–58
Le Bourlot J. 2000. *Astron. Astrophys.* 360:656–62
Le Bourlot J, Le Petit F, Pinto C, Roueff E, Roy F. 2012. *Astron. Astrophys.* 541:A76
Le Gal R, Hily-Blant P, Faure A, et al. 2014. *Astron. Astrophys.* 562:A83
Li X, Arasa C, van Hemert MC, van Dishoeck EF. 2013. *J. Phys. Chem. A* 117:12889–96
Lis DC, Neufeld DA, Phillips TG, Gerin M, Neri R. 2011. *Astrophys. J. Lett.* 738:L6
Lis DC, Phillips TG, Goldsmith PF, et al. 2010a. *Astron. Astrophys.* 521:L26
Lis DC, Schilke P, Bergin EA, et al. 2014. *Astrophys. J. Lett.* 785:135
Lis DC, Wootten A, Gerin M, Roueff E. 2010b. *Astrophys. J. Lett.* 710:L49–52
Liszt H, Lucas R. 1996. *Astron. Astrophys.* 314:917–26
Liszt H, Lucas R. 2002. *Astron. Astrophys.* 391:693–704
Lodders K. 2003. *Astrophys. J. Lett.* 591:1220–47
Lucas R, Liszt H. 1996. *Astron. Astrophys.* 307:237–52
Lucas R, Liszt HS. 2000. *Astron. Astrophys.* 358:1069–76
Luhman ML, Jaffe DT, Keller LD, Pak S. 1994. *Astrophys. J. Lett.* 436:L185–88
Mattila K. 1986. *Astron. Astrophys.* 160:157–70
Melnick GJ, Menten KM, Phillips TG, Hunter T. 1993. *Astrophys. J. Lett.* 416:L37
Menten KM, Wyrowski F, Belloche A, et al. 2011. *Astron. Astrophys.* 525:A77
Merrill KM, Russell RW, Soifer BT. 1976. *Astrophys. J. Lett.* 207:763–69
Meyer DM, Roth KC. 1991. *Astrophys. J. Lett.* 376:L49–52
Monje RR, Lis DC, Roueff E, et al. 2013. *Astrophys. J. Lett.* 767:81
Monje RR, Phillips TG, Peng R, et al. 2011. *Astrophys. J. Lett.* 742:L21
Muller S, Black JH, Guélin M, et al. 2014a. *Astron. Astrophys.* 566:L6
Muller S, Combes F, Guélin M, et al. 2014b. *Astron. Astrophys.* 566:A112
Myers AT, McKee CF, Li PS. 2015. *Mon. Not. R. Astron. Soc.* 453:2747–58
Nagy Z, Van der Tak FFS, Ossenkopf V, et al. 2013. *Astron. Astrophys.* 550:A96
Neill JL, Wang S, Bergin EA, et al. 2013. *Astrophys. J. Lett.* 770:142
Neufeld DA. 2010. *Astrophys. J. Lett.* 708:635–44
Neufeld DA, Black JH, Gerin M, et al. 2015a. *Astrophys. J. Lett.* 807:54
Neufeld DA, Godard B, Gerin M, et al. 2015b. *Astron. Astrophys.* 577:A49
Neufeld DA, Goicoechea JR, Sonnentrucker P, et al. 2010. *Astron. Astrophys.* 521:L10
Neufeld DA, Gusdorf A, Güsten R, et al. 2014. *Astrophys. J. Lett.* 781:102
Neufeld DA, Roueff E, Snell RL, et al. 2012. *Astrophys. J. Lett.* 748:37
Neufeld DA, Wolfire MG. 2009. *Astrophys. J. Lett.* 706:1594–604
Neufeld DA, Wu Y, Kraus A, et al. 2013. *Astrophys. J. Lett.* 769:48
Neufeld DA, Zmuidzinas J, Schilke P, Phillips TG. 1997. *Astrophys. J. Lett.* 488:L141–44
Öberg KI, Boogert ACA, Pontoppidan KM, et al. 2008. *Astrophys. J. Lett.* 678:1032–41
Oka T, Welty DE, Johnson S, et al. 2013. *Astrophys. J. Lett.* 773:42

Omont A, Yang C, Cox P, et al. 2013. *Astron. Astrophys.* 551:A115
Ossenkopf V, Müller HSP, Lis DC, et al. 2010. *Astron. Astrophys.* 518:L111
Pagani L, Roueff E, Lesaffre P. 2011. *Astrophys. J. Lett.* 739:L35
Parise B, Du F, Liu FC, et al. 2012. *Astron. Astrophys.* 542:L5
Peng R, Yoshida H, Chamberlin RA, et al. 2010. *Astrophys. J. Lett.* 723:218–28
Persson CM, Black JH, Cernicharo J, et al. 2010. *Astron. Astrophys.* 521:L45
Persson CM, De Luca M, Mookerjea B, et al. 2012. *Astron. Astrophys.* 543:A145
Persson CM, Olofsson A, Le Gal R, et al. 2016. *Astron. Astrophys.* 586:A128
Phillips TG, van Dishoeck EF, Keene J. 1992. *Astrophys. J. Lett.* 399:533–50
Pilleri P, Fuente A, Cernicharo J, et al. 2012. *Astron. Astrophys.* 544:A110
Pineau des Forêts G, Flower DR, Hartquist TW, Dalgarno A. 1986. *Mon. Not. R. Astron. Soc.* 220:801–24
Pineau des Forêts G, Roueff E, Flower DR. 1986. *Mon. Not. R. Astron. Soc.* 223:743–56
Polehampton ET, Menten KM, Brünken S, Winnewisser G, Baluteau JP. 2005. *Astron. Astrophys.* 431:203–13
Porras AJ, Federman SR, Welty DE, Ritchey AM. 2014. *Astrophys. J. Lett.* 781:L8
Prasad SS, Tarafdar SP. 1983. *Astrophys. J. Lett.* 267:603–9
Rachford BL, Snow TP, Destree JD, et al. 2009. *Astrophys. J. Suppl.* 180:125–37
Rachford BL, Snow TP, Ross TL. 2014. *Astrophys. J. Lett.* 786:159
Rangwala N, Maloney PR, Glenn J, et al. 2011. *Astrophys. J. Lett.* 743:94
Rangwala N, Maloney PR, Glenn J, et al. 2014. *Astrophys. J. Lett.* 788:147
Reid MJ, Menten KM, Zheng XW, et al. 2009. *Astrophys. J. Lett.* 700:137–48
Rist C, Faure A, Hily-Blant P, Le Gal R. 2013. *J. Phys. Chem. A* 117:9800–6
Ritchey AM, Welty DE, Dahlstrom JA, York DG. 2015. *Astrophys. J. Lett.* 799:197
Roueff E, Gerin M, Lis DC, et al. 2013. *J. Phys. Chem. A* 117:9959–67
Roueff E, Lique F. 2013. *Chem. Rev.* 113:8906–38
Roueff E, Lis DC, van der Tak FFS, Gerin M, Goldsmith PF. 2005. *Astron. Astrophys.* 438:585–98
Roueff E, Loison JC, Hickson KM. 2015. *Astron. Astrophys.* 576:A99
Sakai N, Maezawa H, Sakai T, Menten KM, Yamamoto S. 2012. *Astron. Astrophys.* 546:A103
Salyk C, Pontoppidan KM, Blake GA, et al. 2008. *Astrophys. J. Lett.* 676:L49–52
Schilke P, Neufeld DA, Müller HSP, et al. 2014. *Astron. Astrophys.* 566:A29
Schöier FL, van der Tak FFS, van Dishoeck EF, Black JH. 2005. *Astron. Astrophys.* 432:369–79
Sheffer Y, Rogers M, Federman SR, et al. 2008. *Astrophys. J. Lett.* 687:1075–106
Sipilä O, Caselli P, Harju J. 2015. *Astron. Astrophys.* 578:A55
Snow TP, McCall BJ. 2006. *Annu. Rev. Astron. Astrophys.* 44:367–414
Snow TP Jr. 1976. *Astrophys. J. Lett.* 204:L127–30
Solomon PM, Klemperer W. 1972. *Astrophys. J. Lett.* 178:389–422
Sonnentrucker P, Neufeld DA, Phillips TG, et al. 2010. *Astron. Astrophys.* 521:L12
Sonnentrucker P, Wolfire M, Neufeld DA, et al. 2015. *Astrophys. J. Lett.* 806:49
Spilker JS, Marrone DP, Aguirre JE, et al. 2014. *Astrophys. J. Lett.* 785:149
Spitzer L, Drake JF, Jenkins EB, et al. 1973. *Astrophys. J. Lett.* 181:L116
Stäuber P, Doty SD, van Dishoeck EF, Benz AO. 2005. *Astron. Astrophys.* 440:949–66
Sternberg A, Dalgarno A. 1995. *Astrophys. J. Suppl.* 99:565
Sturm E, González-Alfonso E, Veilleux S, et al. 2011. *Astrophys. J. Lett.* 733:L16
Sultanov RA, Balakrishnan N. 2005. *Astrophys. J. Lett.* 629:305–10
Swings P, Rosenfeld L. 1937. *Astrophys. J. Lett.* 86:483–86
Tappe A, Lada CJ, Black JH, Muench AA. 2008. *Astrophys. J. Lett.* 680:L117–20
Thaddeus P, Kutner ML, Penzias AA, Wilson RW, Jefferts KB. 1972. *Astrophys. J. Lett.* 176:L73
Thi WF, Ménard F, Meeus G, et al. 2011. *Astron. Astrophys.* 530:L2
Tizniti M, Le Picard SD, Lique F, et al. 2014. *Nat. Chem.* 6:141–45
Townes CH. 1957. In *Radio Astronomy*, *Proc. 4th IAU Symp.*, ed. HC de Hulst, pp. 92–103. Cambridge, UK: Cambridge Univ. Press
van der Tak FFS, Nagy Z, Ossenkopf V, et al. 2013. *Astron. Astrophys.* 560:A95
van der Tak FFS, Ossenkopf V, Nagy Z, et al. 2012. *Astron. Astrophys.* 537:L10

van der Werf PP, Isaak KG, Meijerink R, et al. 2010. *Astron. Astrophys.* 518:L42
van Dishoeck EF. 1998. In *The Molecular Astrophysics of Stars and Galaxies*, ed. TW Harquist, DA Williams, pp. 53–100. Oxford, UK: Clarendon Press
van Dishoeck EF, Blake GA, Jansen DJ, Groesbeck TD. 1995. *Astrophys. J. Lett.* 447:760
van Dishoeck EF, Herbst E, Neufeld DA. 2013. *Chem. Rev.* 113:9043–85
van Dishoeck EF, Jansen DJ, Schilke P, Phillips TG. 1993. *Astrophys. J. Lett.* 416:L83–86
Vastel C, Ceccarelli C, Caux E, et al. 2010. *Astron. Astrophys.* 521:L31
Vastel C, Phillips TG, Ceccarelli C, Pearson J. 2003. *Astrophys. J. Lett.* 593:L97–100
Vigren E, Zhaunerchyk V, Hamberg M, et al. 2012. *Astrophys. J. Lett.* 757:34
Wagenblast R, Williams DA, Millar TJ, Nejad LAM. 1993. *Mon. Not. R. Astron. Soc.* 260:420–24
Walmsley CM, Ungerechts H. 1983. *Astron. Astrophys.* 122:164–70
Wardle M, Yusef-Zadeh F. 2002. *Science* 296:2350–54
Watson WD, Salpeter EE. 1972. *Astrophys. J. Lett.* 174:321–40
Weinreb S, Barrett AH, Meeks ML, Henry JC. 1963. *Nature* 200:829–31
Weiß A, De Breuck C, Marrone DP, et al. 2013. *Astrophys. J. Lett.* 767:88
Weiß A, Requena-Torres MA, Güsten R, et al. 2010. *Astron. Astrophys.* 521:L1
Weliachew L. 1971. *Astrophys. J. Lett.* 167:L47
Welty DE, Federman SR, Gredel R, Thorburn JA, Lambert DL. 2006. *Astrophys. J. Suppl.* 165:138–72
Whittet DCB, Poteet CA, Chiar JE, et al. 2013. *Astrophys. J. Lett.* 774:102
Wiesemeyer H, Güsten R, Heymick S, et al. 2016. *Astron. Astrophys.* 585:A76
Wirström ES, Charnley SB, Cordiner MA, Milam SN. 2012. *Astrophys. J. Lett.* 757:L11
Wolfire MG, Hollenbach D, McKee CF. 2010. *Astrophys. J. Lett.* 716:1191–207
Wright CM, van Dishoeck EF, Cox P, Sidher SD, Kessler MF. 1999. *Astrophys. J. Lett.* 515:L29–33
Wyrowski F, Menten KM, Güsten R, Belloche A. 2010. *Astron. Astrophys.* 518:A26
Yang C, Gao Y, Omont A, et al. 2013. *Astrophys. J. Lett.* 771:L24
Zanchet A, Agúndez M, Herrero VJ, Aguado A, Roncero O. 2013a. *Astron. J.* 146:125
Zanchet A, Godard B, Bulut N, et al. 2013b. *Astrophys. J. Lett.* 766:80
Zhao D, Galazutdinov GA, Linnartz H, Krełowski J. 2015. *Astron. Astrophys.* 579:L1

RELATED RESOURCES

Online services:

1. The Astrochymist (**http://www.astrochymist.org**) provides the list of detected molecules in the ISM with the associated bibliographic references and related resources in astrochemistry.
2. BASECOL (**http://basecol.obspm.fr/**) is a database devoted to collisional rovibrational excitation of molecules by colliders such as atoms, ions, molecules or electrons.
3. The Leiden Atomic and Molecular Database (LAMDA, **http://home.strw.leidenuniv.nl/~moldata/**) is a database providing the basic atomic and molecular data for molecular excitation calculations.
4. The Virtual Atomic and Molecular Data Centre (VAMDC, **http://portal.vamdc.org/vamdc_portal/home.seam**) is a portal for 29 databases providing atomic and molecular data.
5. The Cologne Database for Molecular Spectroscopy (CDMS, **https://www.astro.uni-koeln.de/cdms**) is a molecular line catalog providing line frequencies, intensities, and molecular partition functions.
6. Jet Propulsion Laboratory Molecular Spectroscopy (**http://spec.jpl.nasa.gov/**) is a molecular line catalog providing line frequencies, intensities and molecule partition functions.
7. Splatalogue (**http://www.cv.nrao.edu/php/splat/**) is a portal to molecular spectroscopy databases.

8. Kinetic Database for Astrochemistry (KIDA, **http://kida.obs.u-bordeaux1.fr/**) is a database of kinetic data. KIDA provides recommendations for a set of important gas-phase chemical reactions.
9. The University of Manchester Institute of Science and Technology Database for Astrochemistry (UDFA, **http://udfa.ajmarkwick.net/**) is a database of kinetic data.
10. The ISM platform (**http://ism.obspm.fr**) provides access to numerical codes and databases of model results, notably the Meudon PDR code and Paris-Durham shock model.